A novel fluoro-electrochemical technique for classifying diverse marine nanophytoplankton

Samuel Barton[1*], Minjun Yang[2], Haotian Chen[2], Christopher Batchelor-McAuley[2, 3], Richard G. Compton[2], Heather A. Bouman[1], Rosalind E.M. Rickaby[1]

[1] Department of Earth Sciences, University of Oxford, South Parks Road, Oxford, OX1 3AN, UK

[2] Physical and Theoretical Chemistry Laboratory, Department of Chemistry, University of Oxford, South Parks Road, Oxford, OX1 3QZ, UK

[3] School of Chemistry, Trinity College Dublin, Dublin 2, Ireland

* Corresponding author: samuel.barton@earth.ox.ac.uk

Pre-print statement:

This is a non-peer reviewed preprint submitted to EarthArXiv.

This preprint has also been submitted to the following journal: *Limnology and Oceanography: Methods*

Abstract

To broaden our understanding of pelagic ecosystem responses to environmental change, it is essential that we improve the spatio-temporal resolution of *in situ* monitoring of phytoplankton communities. A key challenge for existing methods is in classifying and quantifying cells within the nanophytoplankton size range (2-20µm). This is particularly difficult when there are similarities in morphology, making visual differentiation difficult for both trained taxonomists and machine learning based approaches. Here we present a rapid fluoro-electrochemical technique for classifying nanophytoplankton, and using a library of 52 diverse strains of nanophytoplankton we assess the accuracy of this technique based on two measurements at the individual level: charge required to reduce per cell chlorophyll *a* fluorescence by 50%, and cell radius. We demonstrate a high degree of accuracy overall (>90%) in categorising cells belonging to widely recognised key functional groups, however this is reduced when we consider the broader diversity of "nano-phytoflagellates". Notably, we observe that some groups, for example calcifying *Isochrysidales*, have much greater resilience to electrochemically driven oxidative conditions relative to others of a similar size, making them more easily categorised by the technique. The findings of this study present a promising step forward in advancing our toolkit for monitoring phytoplankton communities. We highlight that, for improved categorisation accuracy, future iterations of the method can be enhanced by measuring additional predictor variables with minimal adjustments to the set-up. In doing so, we foresee this technique being highly applicable, and potentially invaluable, for *in situ* classification and enumeration of the nanophytoplankton size fraction.

Introduction

The essential role that phytoplankton play in sustaining marine ecosystems and driving key biogeochemical cycles, notably the biological carbon pump, is unequivocal. As we progress through the Anthropocene, the oceans are facing unprecedented rates of environmental change. In order to improve our global understanding of the impacts that such change is having on phytoplankton communities, and how this might impact key ecosystems services, we must advance our ability to monitor phytoplankton community structure, both spatially and temporally. It is pertinent that *in situ* measurements can capture and quantify the abundance of dominant functional groups of phytoplankton that are present (*i.e.* groups with different biogeochemical and/or ecological functions), as this can inform us about the likely implications of environmental change for marine food webs, biogeochemical cycles, and the capacity of such communities to contribute to sequestration of dissolved CO_2. Widely recognised functional groups, include (but are not limited to): coccolithophores, diatoms, dinoflagellates, and cyanobacteria (Anderson 2005; Nair et al. 2008; Anderson et al. 2021).

An important consideration when attempting to quantitatively assess *in situ* phytoplankton communities is that, as single unicellular organisms, phytoplankton can exhibit a large variation in size, spanning over four orders of magnitude; ranging in length from picophytoplankton <2µm (including most cyanobacteria and picoeukaryotes) to the largest diatoms >1000µm (Snoeijs et al. 2002; Finkel et al. 2010). From an ecological perspective, size is considered a master trait and is known to significantly influence growth rates, nutrient requirements, grazing susceptibility, and sinking rates (Litchman and Klausmeier 2008); all of which have a bearing on important biogeochemical cycles. In this respect, it has been demonstrated that eukaryotic unicells in the nanophytoplankton size range (2-20µm) display the greatest mass-specific metabolic rates, and thus growth rates, relative to larger macrophytoplankton (20µm- 2000µm) and smaller picophytoplankton (Marañón et al. 2013; López-Sandoval et al. 2014; Ward et al. 2017), making them highly competitive and fast responding to environmental perturbations. Indeed, the general success of nanophytoplankton and their ability to dominate phytoplankton biomass has been widely demonstrated from field-based measurements in both the open-ocean (Tarran et al. 2006; Balzano et al. 2012; de Vargas et al. 2015; Bolaños et al. 2020) and coastal waters (Pinckney et al. 2015; Barnes et al. 2015; Alves-De-Souza et al. 2017; Leblanc et al. 2018; Piwosz 2019). Subsequently, as sentinels of the phytoplankton assemblage, nanophytoplankton are an insightful target area for monitoring phytoplankton ecological and biogeochemical functioning in response to ocean change. To date, however, there are numerous constraints and limitations to the available methods in obtaining *in situ* time series measurements of nanophytoplankton diversity and abundance.

Arguably, the most accurate method for quantifying phytoplankton abundance is microscope taxonomy. If specifically focussing on the nanophytoplankton size fraction, taxonomists can quantify abundance to the genus and species level when there are easily identifiable cell characteristics or morphologies (*e.g.* the unique extracellular calcite structures of coccolithophores, or the complex silica frustules of

diatoms). However, this size fraction also contains a large proportion of cell types (typically between 2 and 10µm) that are extremely hard to identify due to their similar morphology and lack of external inorganic structure (Widdicombe et al. 2010; Piwosz 2019). As a result, a significant proportion of the nanophytoplankton fraction is often given the blanket label of 'nano-phytoflagellates' (or similar) in taxonomy surveys. For example, a long-term time series (> 15 years) of the pelagic phytoplankton communities at the L4 station in the Western English Channel has consistently observed that these 'nano-phytoflagellates' make up >80% of the total cell counts per unit volume (Widdicombe et al. 2010). The other main limitations of traditional microscopy are that it is time-consuming in nature, requires highly skilled labour input, and live samples being fixed and preserved prior to analysis.

Flow cytometry is a higher throughput quantitative approach that is often used to distinguish nanophytoplankton and picophytoplankton size fractions, of either live or fixed samples. Light scattering and autofluorescence detection allow for clustering of cells with similar optical properties. This gives a high degree of separation within the picophytoplankton size fraction, as the cyanobacteria autofluorescence and scattering signal is distinct from that of picoeukaryotes. Where cytometry falls short is at being able to fully characterise ecologically relevant components of the nanophytoplankton fraction; only coccolithophores (detectable due to their unique light scattering) and cryptophytes (due to their phycoerythrin content) can be discriminated from other nanoeukaryotes (Tarran et al. 2006; Tarran and Bruun 2015). Thus, in order to obtain a true representation of the species present in the nanophytoplankton fraction, previous studies have often complemented microscope taxonomy and cytometry analyses with genetics-based interpretations (Balzano et al. 2012; Leblanc et al. 2018; Piwosz 2019; Bolaños et al. 2020; Stern et al. 2023), which generally only provide a value for relative abundances.

Over the last decade or so, there has been an emergence of rapid throughput imaging cytometry. This technique demonstrates a high degree of accuracy in classifying phytoplankton cell types from a combination of image-based machine learning and autofluorescence measurements (Olson and Sosik 2007; Sosik and Olson 2007; Dugenne et al. 2014; Álvarez et al. 2014; Camoying and Yñiguez 2016; Fragoso et al. 2019) ; thereby, in essence, merging the identification skills of a microscope taxonomist, with the speed and tools of a flow cytometer. FlowCam (Yokogawa Fluid Imaging Technologies, Inc) is a laboratory-based device that has been shown to produce highly comparable results when validated alongside traditional microscopical estimates (Álvarez et al. 2014) and, depending upon the FlowCam model, can analyse a broad range of particle sizes from 300nm to 1mm. As with microscope techniques however, the current models of FlowCam still struggle to correctly classify nanophytoplankton that have similar sizes and morphologies; any machine-based learning that is relied upon for image analysis is only as good as the human interpretation that drives the training, along with the resolution of the images acquired. The Imaging FlowCytobot (McClane Research Laboratories, Inc) and CytoBuoy (CytoBuoy b.v.) are devices that operate similarly but have been developed to function autonomously

at sea (Olson and Sosik 2007; Fragoso et al. 2019). Whilst these are promising steps forward for the generation of *in situ* temporal and spatial understanding of phytoplankton community structure, the imaging on these devices is optimized to the larger phytoplankton size range, with the Imaging FlowCytobot capturing between 10 and 100µm cell lengths, and the CytoBuoy from 1µm to 778µm but with reported poor resolution at the lower limits necessary for categorising nanophytoplankton (Dugenne et al. 2014; Fragoso et al. 2019). Subsequently, to-date, imaging flow cytometry methods struggle to fully capture and classify a large proportion of the phytoplankton communities that is in the nanophytoplankton range. We therefore identify that a key challenge in monitoring the health of pelagic ecosystems is in developing novel high-throughput techniques that allow for higher resolution *in situ* discrimination and quantification in the nanophytoplankton size range.

Moving forward, recent developments in the field of analytical chemistry have shown that electrochemically induced oxidative stress destroys phytoplankton chlorophyll *a* fluorescence in a manner that is idiosyncratic, allowing for differentiation of phytoplankton species from measurements that are obtained within 10s of seconds (Yang et al. 2019; Yu et al. 2022). When a sufficiently high potential is applied to an electrode that is immersed in seawater, a wide range of oxidants can form and diffuse from the electrode surface, for example; oxidation of water to hydrogen peroxide and hydroxyl radicals, bromide to hypobromous acid, and chloride to dichlorine (Yang et al. 2019; Yu et al. 2022). The subsequent reaction of these oxidants with phytoplankton is seen to cause a rapid decay of the cellular chlorophyll *a* fluorescence signal. The rate at which this happens is dependent on a number of factors, including; the distance of the phytoplankton cells from the electrode, the potential applied (and thus the species and concentration of oxidants generated), and more importantly for the work presented here – the type of phytoplankton cell. To that end, we apply this novel fluoro-electrochemical method to a much broader suite of ecologically relevant pico- and nanophytoplankton (52 cultured strains) to produce a 'susceptibility library' based on two variables; chlorophyll *a* fluorescence 'switch-off' and measured cell radius. This library is assessed using a random forest approach to determine how well the electrochemical method can be used to classify cells into relevant groups. We specifically focussed on strains of nanophytoplankton that (a) represent key functional groups and (b) represent some of the traditionally hard to identify "nano-phytoflagellates". We then explore a possible biological underpinning to the method, as well as discussing its current limitations and suggested improvements.

Methods and Procedures

Culturing for the 'susceptibility library'

Phytoplankton monocultures were selected so that we had a good representation of each of the key functional groups (37 strains in total), along with an assortment of strains that we consider to be likely 'nano-phytoflagellate' candidates (15 strains in total, within the 2 to 10µm size range). The key functional groups that we analyse are herein labelled as: "Calcifying Isochrysidales" (7 strains), "Coccolithophores" (8 strains), "Diatoms" (10 strains), "Dinoflagellates" (8 strains), and "Picophytoplankton" (4 strains). In this instance, "Calcifying Isochrysidales" includes strains of both *Emiliania huxleyi* (7 strains) and *Gephyrocapsa oceanica* (1 strain). Whilst they might both be considered coccolithophores, given their cosmopolitan nature and the fact they are the most globally abundant calcifiers (particularly *E. huxleyi*) we considered them as a separate group for this analysis. We also chose to include a range of *E. huxleyi* cell stages (both calcified and non-calcified diploid strains, along with a haploid strain) and morphologies (representing different extents of calcification), allowing us to robustly investigate the within species variance in the electrochemical susceptibility. Picophytoplankton are included to allow us to test the lower size limits for detection and classification of our method, including two strains of cyanobacteria (both *Synechococcus* sp.) and two pico-eukaryotes (*Micromonas pusilla* and *Ostreococcus tauri*). Broadening the dataset to encompass nanophytoplankton beyond the key functional groups, the additional groups in our analysis were as follows: "Eustigmatales" (1 strain), "Green algae" (3 strains), "Non-calcifying Isochrysidales" (4 strains), "Pavlovales" (3 strains), "Phaeocystales" (1 strain), and Prymnesiales (3 strains). These strains were selected as it has previously been noted that the unrecognisable "nano-phytoflagelletes", which are a challenge for microscope taxonomy, could broadly be assigned to the phyla of haptophytes (non-calcified types), chlorophytes (or green algae), and cryptophytes (Piwosz 2019). A full list of the 52 strains used in this study can be found in SI Table S1. In the case of "Eustigmatales" we assume that a single strain of *Nannochloropsis granulata* is broadly representative, and for "Phyaeocystales" we worked with a single strain of *Phaeocystis globosa*.

All strains were obtained from reputable culture collections: Roscoff Culture Collection (Roscoff, France), Culture Collection of Algae and Protozoa (Oban, UK) and The Marine Biological Association (Plymouth, UK). Following their arrival, they were maintained in exponential growth through regular sub-culturing under sterile conditions on their advised growth medium (see Table S1, SI). All growth media were prepared using synthetic ocean water (Morel et al. 1979), allowing greater control over the main composition of the seawater (see Table S2, SI), and thus consistency in the probable oxidants formed when measuring the electrochemical responses. Cultures were incubated in PHCbi MLR-352-PE Incubators (PHC Europe B.V.) set to 17ºC (or 20 ºC for all diatoms), with a 14:10h light-dark regime at a PAR intensity of 20-40µmol m^{-2} s^{-1}, and were kept under these conditions for a minimum of two

months prior to carrying out the electrochemical susceptibility measurements. The growth of the cultures was tracked on a daily basis using a TECAN Spark plate reader (Tecan Group Ltd.), where three technical replicates of 200µl of each culture were measured for chlorophyll *a* fluorescence as a proxy for culture biomass. We then selected a time-point in mid-exponential growth phase, when each strain was not at saturation point (*i.e.* carrying capacity) and therefore not nutrient limited, to conduct our experiments (see Figure S1, SI). Immediately prior to the electrochemical experiments, to obtain a sufficient number of cells per image series (as described below), all strains were concentrated by centrifugation (Centrifuge 5702, Eppendorf UK Limited) at 1000 r.p.m for ten minutes, and resuspended to a concentration typically ranging between 5 and 10x.

The fluoro-electrochemical technique

A more detailed description of the fundamental electrochemical principles and details of the underlying methodology, including specifics of the equipment used, can be found in the previously published work by Yu *et al.* (2022). For the purposes of this study, the step-by-step method described below outlines the essential procedures that were followed to yield the underlying dataset for the susceptibility library. In summary, we used a galvanostat based ramping linear current, applied to phytoplankton cells settled onto the surface of a carbon electrode surface (thus controlling for distance from the electrode) and monitored chlorophyll *a* fluorescence decay over time per individual cell (see Table S3 for number of individual cell measurements per strain). The constant rate of current ramping (10µA s^{-1}) means that the moles of oxidant being generated electrochemically increases with time in a controlled fashion. This approach allows for greater possible discrimination of phytoplankton cell types and over a shorter experimental time frame (e.g. 10s of seconds), as opposed to running experiments at a single set potential. Consequently, as cell types have different levels of resilience to such oxidative stress, this technique enables us to quantify the differences in time that is required to drive the chlorophyll *a* quenching across the phytoplankton investigated.

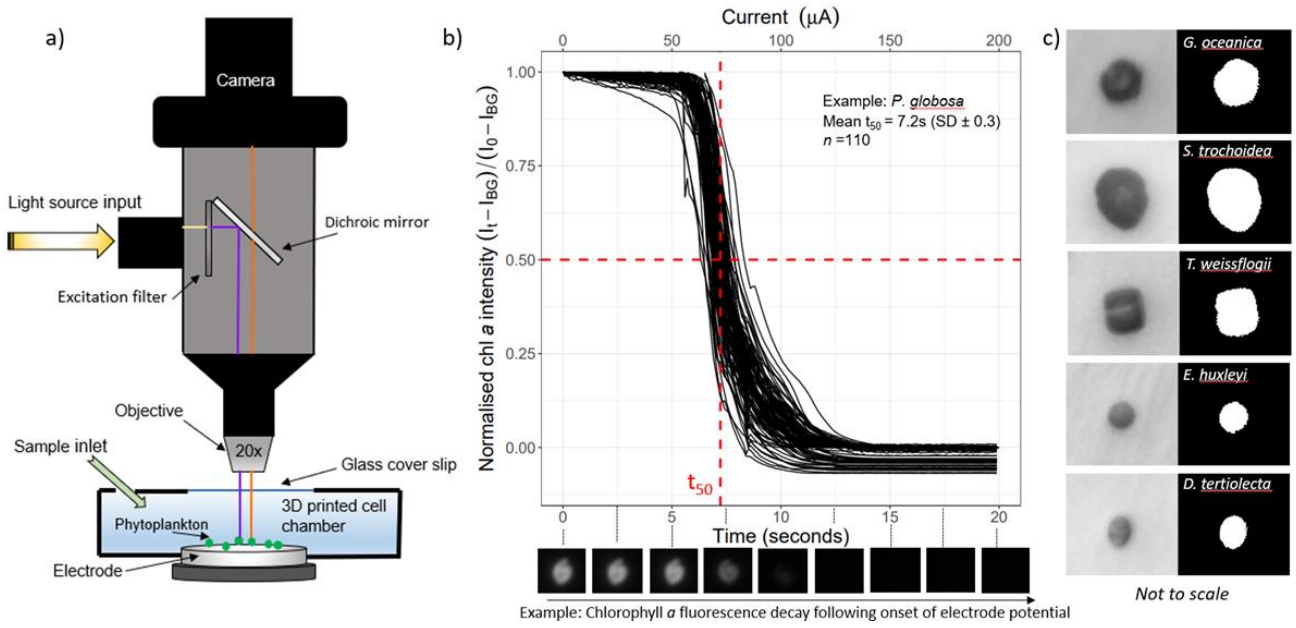

Figure 1. **(a)** a simple schematic diagram of the electrochemistry – fluorescence microscope set up adapted from Yu *et al.* (2022), **(b)** an example of normalised Chlorophyll *a* fluorescence transient data for the species *Phaeocystis globosa*, following onset of the potential and with a current ramping of 10µA s^{-1}. Each black line represents a single cell measurement (n = 110), and the dashed red markings highlight the time point, t_{50}, where normalised fluorescence values have been reduced by 50%. The time-series of images below the plot illustrate the loss of fluorescence with time for one individual cell. **(c)** examples of brightfield images taken before the electrochemical experiments for a selection of strains (left column), and the respective estimate of projected pixel area that was subsequently used to determine the effective radius of each cell (after assuming a circular shape).

The fluoro-electrochemical measurements were made as follows (See Figure 1.a, adapted from Yu *et al.* 2022).

1) A concentrated sample from a phytoplankton monoculture in exponential growth phase (as described in Culturing section above) was 'drop cast' onto the surface of the working electrode. After ~1 minute of allowing the cells to be deposited on the surface, excess solution was gently drawn-off using a tissue. Immediately following this, the 3D printed cell chamber was filled up to maximum capacity with culture growth medium via the sample inlet. Once the chamber was at capacity a glass cover slip was put in place.
2) Using the fluorescence microscope (Axio Examiner, Carl Zeiss Ltd., Cambridge U.K.), we focussed on a field of view whereby we had a high proportion of phytoplankton cells on the electrode surface (mean number per experiment = 23 ± 18 S.D., across 212 unique experimental image series).
3) With the microscope set in a bright-field mode, we took an image of the starting positioning of the cells. These images were later used to obtain an estimate of effective cell radius (see Figure. 1b).
4) Next, switching the microscope to fluorescence mode, the cells were excited using a 475 ± 35nm excitation filter and emission signal passed through a dichroic mirror specific to

wavelengths >590nm for chlorophyll *a* fluorescence detection. Simultaneously, the galvanostatic control was synchronised with the camera and data acquisition was started. For the first 40s of the electrochemical experiment no potential was applied, allowing the fluorescence signal to stabilise. Following this, the current was ramped from 0µA at a rate of 10µA s^{-1} and images recorded at a capture rate of 10f.p.s. For each set of experiments the current was ramped until the chlorophyll signal had completely 'switched off'.

5) After the experiment, the 3D chamber was rinsed clean with DI water and the above steps were repeated a minimum number of 3 times for each phytoplankton strain.

Following the experimental data collection, the raw fluorescence transient data was processed for each individual cell within each experimental time-series (n = 4884, across all strains) using ImageJ software (v1.53c, Fiji distribution), where "n" is the number of individual phytoplankton cell measurements. The integrated fluorescence intensity values for each individual cell (I_t) were corrected by subtracting the background signal of the electrode surface (I_{BG}) for all time points: $I_t - I_{BG}$, following this all values were then normalised by dividing by the fluorescence intensity at the onset of the potential (I_0): $(I_t - I_{BG}) / (I_0 - I_{BG})$. We then used the normalised transient data to determine the time-point for each individual cell where normalised intensity had decreased by 50% (t_{50}), see Figure 1.b. Due to the consistent linear ramping of current at 10µA s^{-1} and that all phytoplankton cells imaged were settled on the surface of the electrode within the timescale of the experiments, we were able to determine the total charge required to be injected to reach t_{50} for each cell, and thus we herein refer to our chlorophyll *a* susceptibility factor as charge at t_{50} (in mC). In some instances where there was significant movement of individual cells it was not possible to accurately measure the chlorophyll *a* fluorescence profile throughout the time series, and subsequently data for these cells was considered erroneous and removed from the analysis.

For each cell specific chlorophyll *a* transient, we used the corresponding bright-field image collected prior to electrochemical experiments to derive a corresponding cellular area based on white pixel area of the cell (Figure. 1c). This was achieved by using the auto-threshold function in ImageJ freeware. From the total pixel area and using a predefined µm to pixel ratio (0.31µm per pixel), we were able to estimate an effective radius (in µm) of each cell by assuming a circular 2D cell geometry (or a spherical cell). For cells in the picophytoplankton size range, due to the lack of contrast with the electrode surface it was not possible to accurately distinguish cell area, and therefore in these instances we obtained a measurement of mean cell pixel area by manually measuring the area of a subset of at least 10 cells per experimental time-series (using ImageJ).

Assessment of the susceptibility library

With the two parameters of charge at t_{50} (mC) and effective radius (µm) defined for each individual cell, we assessed the applicability of the susceptibility library for distinguishing the cells into pre-defined groupings of relevance, as defined in the Culturing section above. Prior to this assessment it was necessary to balance the dataset for even strain representation within each pre-defined grouping. This was necessary as there was limited control over the number of individual cell transients obtained per experimental image series per strain, resulting in under/over-representation within groups (see Tables S3 and S4, SI). To balance the data at the group level, we identified the strain within each group that had the lowest number of observations, and used that minimum number to randomly subset a sample of the same length for each of the other strains within the grouping level. This was achieved using the "*sample_n*" function in the R package "*dplyr*" (R version 4.2.2). The resultant balanced dataframe (n = 2277) was subsequently used to derive mean values at the group level and for the analyses described below. See Tables S5 and S6 for balanced data.

First, looking at charge at t_{50} independently from radius, across all strains (unbalanced dataset) we see a large range spanning three orders of magnitude (see Figure S3 and Table S3, SI), from a mean of 0.08mC (±0.02 S.D.) for the pico-eukaryote *Ostreococcus tauri*, up to 7.69mC (±1.89 S.D.) for the dinoflagellate *Scripsiella trochoidea*. At the level of the pre-defined groupings described above (balanced dataset) we see the lowest mean charge at t_{50} within the "Picophytoplankton" of 0.11mC (±0.03 S.D.), and the greatest mean charge at t_{50} within the "Eustigmatales" 2.45mC (±0.41 S.D.), preceded by "Dinoflagellates" at 2.33mC (±2.37 S.D.) (see Figure S4 and Table S6, SI). The large range in these values indicate that there is a strong effect of cell grouping on the resilience to electrochemically driven oxidative stress. Critically, however, there is also considerable overlap in the values, as an example: "Calcifying Isochrysidales" have a mean charge at t_{50} of 1.42mC (±0.58 S.D.), which sits well within the large deviation range of the "Dinoflagellates". Subsequently, in order to further distinguish the groupings in such instances, use of the effective radius can provide an additional dimension for separation where there is overlap. In the case of the previous example, we see that "Calcifying Isochrysidales" have a mean effective radius of 3.36µm (±0.88 S.D.), whereas "Dinoflagellates" have a significantly larger mean effective radius of 10.03µm (±3.04 S.D.) (see Figure S5, SI). Taking this forward, we next use a random forest analysis to test the potential for single cell categorisation across all of the groups based on the variance in both charge at t_{50} and effective radius.

Random forest analysis uses the pre-defined classes (in this case the phytoplankton groupings) to construct a range of 'decision trees' for discrimination of the individual observations (in this case each phytoplankton cell) based upon the predictor variables (in this case charge at t_{50} and effective radius) of a dataset. To effectively test the accuracy of classification, this requires input of a 'training' dataset so that the random forest algorithm can create the necessary discrimination functions for the pre-defined classes. A 'testing' dataset can then be used to determine the accuracy of the discrimination on an

independent set of 'blind' observations. As an example of its application in a relevant field, random forest algorithms have previously been used to successfully distinguishing individual populations of phytoplankton strains from flow cytometry measurements on artificial communities (Bestion et al. 2020, 2021). Whilst a flow cytometer records a wide range of fluorescence and light scattering variables per individual cell, here we are limited to testing the distinguishing power of our method with only the two aforementioned predictor variables. Specifically, for our analysis, we used the "randomForest" function in the R package "randomForest"; this function uses Breiman's random forest algorithm for classification (Breiman 2001). From this we could determine categorisation 'decision trees' for four subsets of the susceptibility library data: (a) The key functional groups only (37 strains, 5 groups) with both unbalanced (see Figure 2) and balanced datasets (see Figure S6, SI), and (b) all groups (52 strains, 11 groups) with both unbalanced data (see Figure 3) and balanced data (see Figure S7, SI). For each subset, we randomly split the datasets using the "*sample_n*" function as described above, assigning 80% of data for the training component, and 20% for the testing. The two input predictor variables of charge at t_{50} and effective radius were natural log transformed prior to running the analysis. For both the training and testing steps, an overall "out-of-bag" error was returned to demonstrate the success rate of the categorisation using discrimination functions derived for each subset of the data. Similarly, for each subset, the level of success rate in correctly classifying cells to each of the groupings was also derived.

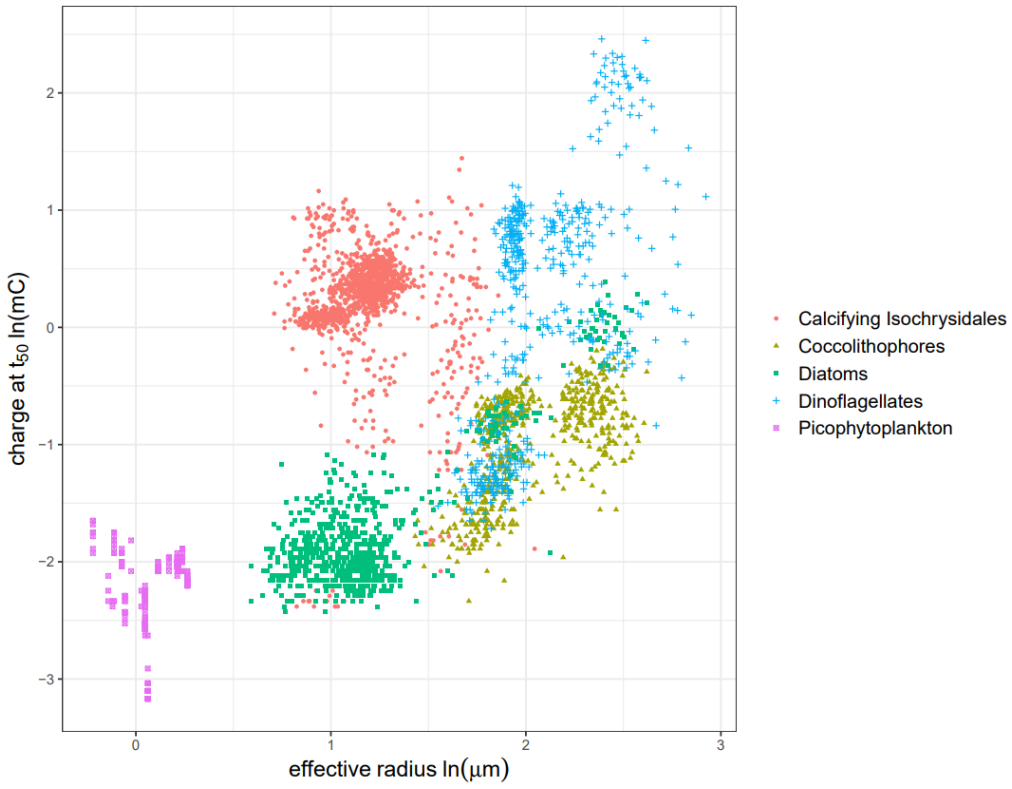

Figure 2. A scatterplot of natural log charge at t_{50} (mC) against natural log effective cell radius (µm) for the 'key functional groups' of cells measured in this study (n = 3880, see Table S4 for a summary of the data presented here). Whilst there is some overlap of the groupings, the random forest analysis on the balanced version of this dataset returned an overall accuracy of 91.5% with the training data and 90.6% with the testing (see Tables 1 and S9).

Table 1. Results from training the random forest using the balanced subset of data for the key groups only (*n* = 1406). The green highlighted grid squares indicate the number of successful categorisations for each group within the training. Overall "out-of-bag" error was 8.5% (thus 91.5% overall accuracy). The follow-up testing on an independent 'blind' subset of observations yielded an overall 90.63% accuracy.

		Predicted (Training)					
		Calcifying Isochrysidales	Coccolithophores	Diatoms	Dinoflagellates	Picophytoplankton	Accuracy (%)
Actual (Training)	Calcifying Isochrysidales	421	4	7	2	0	97
	Coccolithophores	2	225	12	5	0	92.2
	Diatoms	4	23	268	7	0	88.7
	Dinoflagellates	1	15	10	54	0	67.5
	Picophytoplankton	0	0	0	0	26	100
						Overall Accuracy (%)	91.5

At the level of key functional groups, and with the balanced dataset, we found there to be an overall accuracy of 91.5% following the initial training stage (see Table 1), and 90.6% after using the trained discrimination functions on a testing dataset (see Table S9). The unbalanced dataset yielded overall accuracies of 90.9% and 90.0%, respectively (see Tables S7 and S8), indicating that with the balanced data there was a slight improvement of accuracy. The high level of accuracy is perhaps unsurprising considering the visual clustering of the datapoints (see Figure 2). Within the groupings however, some classifications perform better than others. "Picophytoplankton" are correctly classified in all instances (100%), and this is driven by their much smaller size relative to the others. "Calcifying Isochrysidales" are predicted with 97% accuracy, and this appears to primarily be driven by their greater electrochemical resilience (*i.e.* greater charge at t_{50}) relative to cells of a similar size. The lowest level of accuracy was in classifying "Dinoflagellates", with a training accuracy of 67.5% and a testing accuracy of 58.3%. This is due to a considerable variation in the charge at t_{50} within this group, meaning that some strains of dinoflagellate are misclassified as larger diatoms and coccolithophores. On the whole, the fact that there is >85% accuracy in the classification of four out five of the key groups is indicative that the electrochemical sensitivity is providing a good degree of separation, in combination with size. Nonetheless, in order to be more reflective of the diversity of nanophytoplankton found in naturally occurring communities, we next consider the level of performance once all of the other groups are considered in the random forest analysis (see Figure 3).

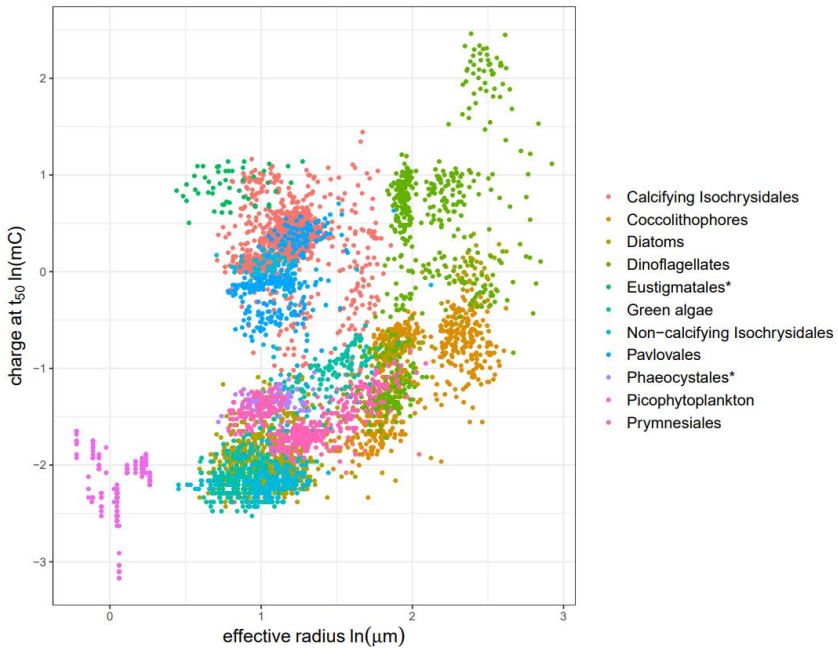

Figure 3. A scatterplot of natural log charge at t_{50} (mC) against natural log effective cell radius (µm) for all groups of cells measured in this study (n = 4884, see Table S4 for a summary of the data presented here). Compared to Figure 2, where just the key functional groups are presented, we now see more overlap of the groupings. The random forest analysis on the balanced version of this dataset, where strain representation within each group was standardised, returned an overall accuracy of 69.1% with the training data and 71.7% with the testing (see Tables 2 and S12).*denotes groups that were just represented by a single species.

Table 2. Results from training the random forest using the balanced subset of data for all groups (n = 2277). The green highlighted grid squares indicate the number of successful categorisations for each group within the training. Overall "out-of-bag" error was 30.9%. The follow-up testing on an independent 'blind' subset of observations yielded an overall 71.7% accuracy. *denotes groups that were just represented by a single species.

		Predicted (Training)											
		Calcifying Isochrysidales	Coccolithophores	Diatoms	Dinoflagellates	Eustigmatales*	Green algae	Non-calcifying Isochrysidales	Pavlovales	Phaeocystales*	Picophytoplankton	Prymnesiales	Accuracy (%)
Actual (Training)	Calcifying Isochrysidales	367	2	1	2	4	6	26	21	1	0	4	84.6
	Coccolithophores	1	210	12	3	0	0	0	0	0	0	18	86.1
	Diatoms	1	22	183	7	0	3	33	0	9	0	44	60.6
	Dinoflagellates	2	11	10	53	0	0	0	0	0	0	4	66.3
	Eustigmatales*	13	0	0	0	26	0	0	0	0	0	0	66.7
	Green algae	6	1	9	0	0	13	5	0	0	0	8	31
	Non-calcifying Isochrysidales	42	0	47	1	0	2	47	6	1	0	2	31.8
	Pavlovales	36	0	1	0	0	0	1	84	1	0	1	67.7
	Phaeocystales*	1	0	4	0	0	1	1	0	44	0	37	50
	Picophytoplankton	0	0	0	0	0	0	0	0	0	29	0	100
	Prymnesiales	1	13	29	1	0	3	0	0	33	0	183	69.6
								Overall accuracy (%)					69.1

When all of the groupings are considered, the overall accuracy was 69.1% following the initial training stage (see Table 2), and 71.7% after using the trained discrimination functions on a testing dataset (see Table S12). The unbalanced dataset yielded overall accuracies of 71.9% and 72.9%, for training and testing respectively (see Tables S10 and S11). The lower level of accuracy compared to the interpretation with only the key groups is perhaps unsurprising given that the number of potential classes in the random forest has more than doubled (5 to 11) and considering the greater extent of overlap in the group level clustering of the datapoints (see Figure 3). Despite the overall reduction in accuracy, many of the key groups maintain a relatively high level of predictability with four out of the five returning training accuracies of more than 60%. Of the key groups, the biggest reduction in accuracy is in the "Diatom" group, now 60.6% in training and 55% in testing. An element of confusion in this instance is being caused by cell types belonging to the other groups, such as "Non-calcifying Isochrysidales" and "Prymnesiales", which have similar size and electrochemical susceptibility distributions. Of the additional groups, the best performing are the "Prymnesiales" at 69.6% in training and 81.6% in testing, along with "Pavlovales" at 67.7% and 69.1%. The worst performing were, "Green algae" received a training accuracy of 31%, with most of the confusion being with "Diatoms". "Non-calcifying Isochrysidales" also had a training accuracy of 31.8%, with considerable confusion coming from both "Diatoms" and "Calcifying Isochrysidales".

Significantly, of the key groups, there were some notable high performers in testing accuracy despite the inclusion of the other groupings: "Calcifying Isochrysidales" 89.7%, "Coccolithophores" 80.3%, and "Picophytoplankton" remained at 100%. In the case of the "Coccolithophores" it seems to be due to their low electrochemical resilience relative to their large size, in contrast to "Dinoflagellates" of a comparable size which generally have a greater resilience. "Calcifying Isochrysidales" on the other hand appear to be highly distinguishable for their remarkable electrochemical resilience relative to other groups of a similar size. This poses some key questions about the underlying mechanism of this technique for distinguishing cell types across the groups: How much is cell size driving the electrochemical resilience? Are there any contradicting exceptions to any potential size scaling? With this in mind, we next scrutinise the effect of size on the susceptibility factor to see how much this is driving the overall resilience to the oxidative stress across the groups.

Understanding the mechanism: the size scaling of the relationship and size adjusted resilience

Using the balanced dataset of all groupings, we investigated if there was a significant linear relationship between natural log transformed charge at t_{50} and effective radius (see Figure 4). This was achieved using the '*lme4*' package in R for linear mixed effects modelling, whereby we fitted and compared linear models to the data both with and without the random effect of grouping on both the intercept and slope of the response. Of the two models, the model including the random effect of grouping on both

the slope and intercept scored more favourably than the model without (see Table S13, SI), indicating that there was an overall significant positive linear scaling between charge at t_{50} and effective radius (p <0.001), but that this scaling was highly variable across the groupings. The overall model returned a slope value of 0.76 (95% CIs: 0.34 – 1.16). Out of the 11 'groups', 7 of them had significant positive within group size dependence, notably "Green algae", "Diatoms", and "Dinoflagellates" had particularly strong scaling of more than 1 (See Figure S8, SI and Table S14, SI). There was no significant size scaling within the groups of "Eustigmatales", "Phaeocystales" and "Picophytoplankton"; and this is perhaps unsurprising given that the latter two were only represented by one single strain. Notably, the only group that had a significant negative size scaling were the "Calcifying Isochrysidales", -0.33 (95% CIs: -0.50 – -0.16).

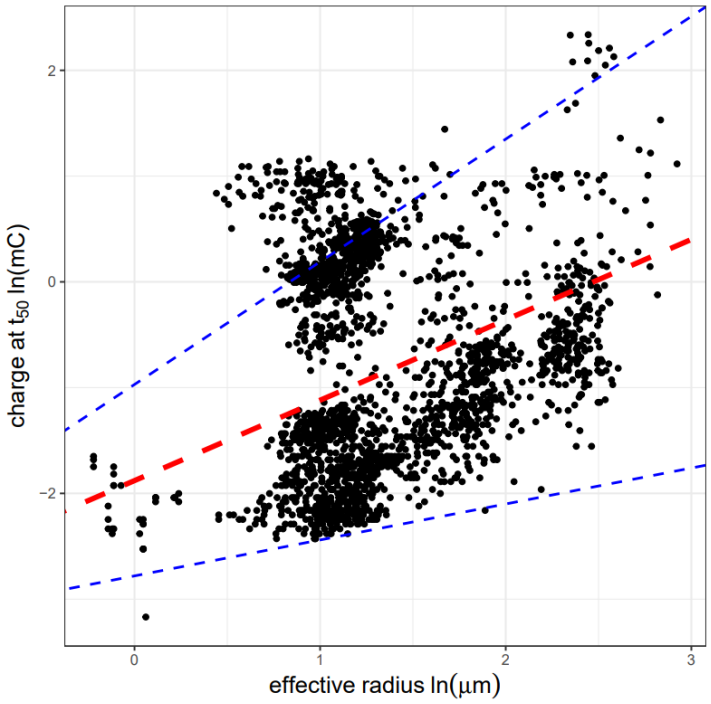

Figure 4. A scatterplot of natural log charge at t_{50} (mC) against natural log effective cell radius (µm) of cells measured in this study, following the balancing of strain representation per group (n = 2277, see Table S5 SI for raw data presented here). The red line indicates the overall slope (0.76) of the allometric relationship modelled using linear mixed effects with the random effect of grouping on the slope and intercept factored for, and the blue dashed lines indicate the 95% confidence of this model fit (slopes of 0.34 and 1.16 for lower and upper, respectively). See Tables S13 and S14, SI.

On the whole, what this demonstrates is that across most of the groupings there is an intrinsic allometric scaling of charge required to "switch-off" the chlorophyll *a* signal. This was previously found at the species level in a recent study by Yu *et al*. (2023), which demonstrated that differing electrochemical susceptibility of life stages of *Chlamydomonas concordia*, were primarily driven by size variation in the different cell types, and not an underlying biological factor (Yu et al. 2023). Consequently, we could postulate that any significant differences in electrochemical susceptibility following a size normalisation might therefore indicate which of the groupings in this study have an underlying

biological feature that results in higher or lower resilience. We investigated this by normalising all charge at t_{50} values for size, by simply dividing charge (mC) by effective radius (µm) for each of the individual measurements in the balanced dataset (see Figure 5).

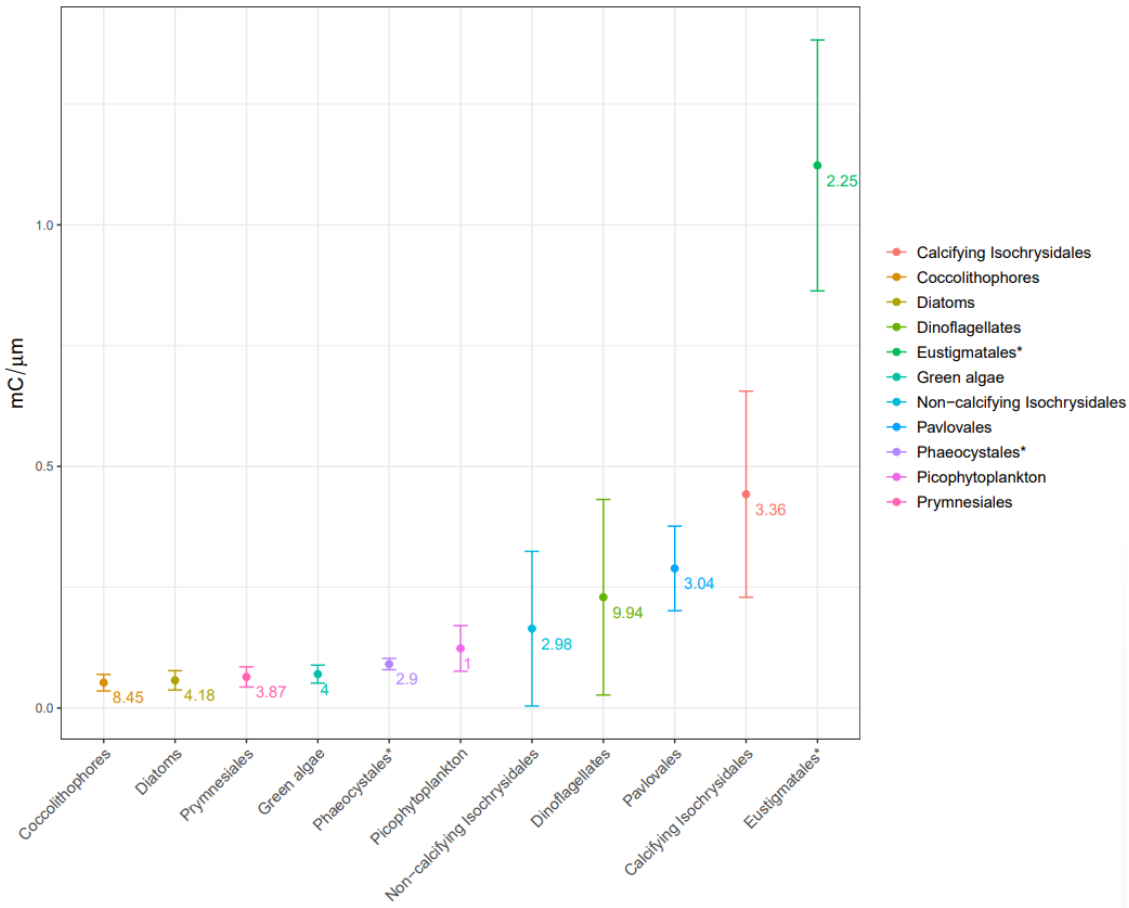

Figure 5. Comparison of per group means of size normalised charge at t_{50}. Data points represent the mean value for each group and the error bars are for standard deviation, following balancing the representation of the individual strains within each group. The labelled numbers alongside the data points represent the mean effective radius for each of the groups, illustrating that in some instances there is a disproportionate resilience to the electrochemical charge relative to cell size – notably for "Calcifying Isochrysidales" and "Eustigmatales". For pairwise comparisons see Table S15, SI.

Following size normalisation of the charge at t_{50}, we carried out pairwise comparisons across the groups using Pairwise Wilcoxon Rank Sum testing (due to the non-parametric distribution of data in most of the groups), for this we used the function "*pairwise.wilcox.test*" in the R package "*stats*", with "*p.adjust.method*" set to the "Bonferroni" correction of *p* values see Table S15, SI. We see no significant difference between a number of the key groupings, notably "Diatoms" and "Coccolithophores" (p = 0.065), and "Picophytoplankton" and "Dinoflagellates" (p = 0.423). Given that "Diatoms" in this dataset have a mean effective radius of 4.81µm (±2.59 S.D.) and "Coccolithophores" of 8.43 µm (±2.21 S.D.), this indicates that most distinguishing between these two groups must primarily be driven by size, given that their size normalised charge values are

indistinguishable. Likewise, "Picophytoplankton" have a mean effective radius of 1.02 µm (±0.15 S.D.) and "Dinoflagellates" a mean effective radius of 10.03 µm (±3.04 S.D.), demonstrating extreme ends of the size spectrum within this dataset, yet after size normalisation of their respective charge values they are indistinguishable in terms of their electrochemical resilience. Contrary to these observations, it is evident that there are some clear outliers, whereby following size normalisation they are more distinguishable from the rest of the groups, notably "Calcifying Isochrysidales" and "Eustigmatales". In both cases, their size normalised charge was statistically greater than all the other groups, with "Eustigmatales" having the greatest resilience overall (see Figure 5, and Table S15). Whilst we only have one strain representing "Eustigmatales" in this dataset, *Nannochloropsis granulata*, we might infer that there is something about the particular biology of these two groups that is driving their greater resistance to the high levels of oxidative stress. This is of relevance to the method, because across all our assessments using the random forest analysis it was the "Calcifying Isochrysidales" group that consistently retained the highest level of prediction accuracy of all the key functional groups. Taking our investigation further, we next take a closer look at within species variability to disentangle if any of the particular strains of *E. huxleyi*, representing different life stages and calcification morphologies (Green et al. 1996; Young et al. 2003; Bendif et al. 2023), can help to identify any further trends that may lead to understanding the biological mechanism (see Figure 6).

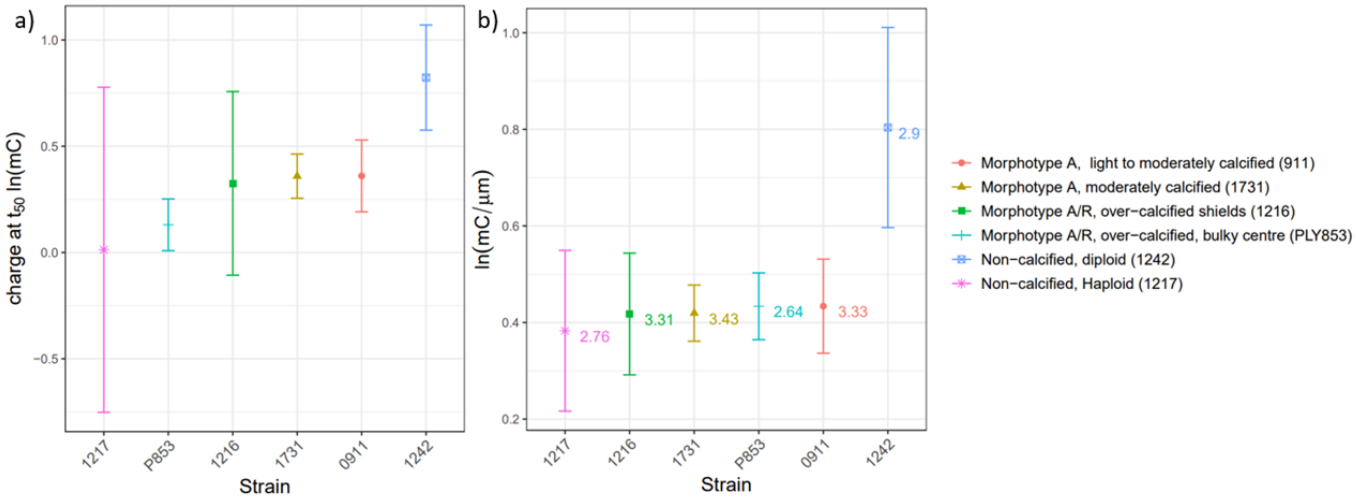

Figure 6. (a) Comparison of natural log transformed mean charge at t_{50} across the different strains of *E. huxleyi* representing different coccosphere morphologies (P853 (PLY853), 1731 (RCC1731), 0911 (RCC911), 1216 (RCC1216)) and non-calcified life stages (1217 (RCC1217), 1242 (RCC1242)), for details on the strains see Table S1, **(b)** Comparison of natural log transformed size normalised charge across the same strains. Data points represent the mean value for each group and the error bars are for standard deviation. The labelled numbers alongside the data points represent the mean effective radius for each of the strains, illustrating that across the strains there is minimal difference in size. For pairwise comparisons see Table S16, SI.

Despite their differing coccosphere morphologies (ranging from light-, moderate-, and over- calcified features), across the four calcified (diploid) strains there was negligible difference in the size normalised charge at t_{50} (See Figure 6, and Table S16). This result is reassuring in terms of the proposed sensing technology, as it suggests that the within strain variance of "Calcifying Isochrysidales" is not too substantial to cause confusion with other strains/groups. Of particular curiosity, the '1242' non-calcified diploid strain (RCC 1242), had a significantly greater charge per unit size relative to all other strains, and furthermore the '1217' non-calcified haploid strain (RCC 1217) was generally indistinguishable from the calcified strains (except for its calcified diploid version RCC 1216). This observation is of relevance to understanding any potential underlying mechanism to the sensor technology for two reasons. Firstly, it indicates that there is minimal effect of the extracellular inorganic calcite layers in either increasing or reducing the resilience of the cell type. This is also more broadly demonstrated when comparing the "Calcifying Isochrysidales" group to the "Coccolithophores", the latter in many instances (*e.g. Coccolithus braarudii*) having much larger extracellular calcium carbonate shell volumes (Yang et al. 2022), yet relatively much faster "switch-off" times under this method (See Figure S10, SI). Secondly, it suggests that there is something biologically different between the non-calcified and calcified diploid cells that is driving the discrepancy in the resilience. Disentangling this is beyond the scope of this study, but presents an avenue for further investigation as to why such cell types have greater resilience. Indeed, along a similar vein of thinking, exploring the biological differences of each of the groups against the highly resilient *Nannochloropsis granulata* could help to understand what is driving such resilience irrespective of the cell size. As a tentative suggestion, greater resilience could simply be determined by the membrane structure of the cell, whereby the presence of more membrane layers surrounding the cytoplasm and/or the plastids could potentially present a barrier acting to slow down the transmission of the oxidative radicals to the chlorophyll molecules (Yu et al. 2022). It has previously been reported that *Isochyrsidales* (and specifically *E. huxleyi* and *G. oceani*ca) are distinctive from other coccolithophorids due to a number of different periplast and membrane features, including: unmineralized outer cell scales, more rigid double membrane structures of the peripheral endoplasmic reticulum, and unique long-chain membranous alkenones (Fujiwara et al. 2001). Perhaps it is features, such as these, slowing the transmission of radical oxidants to the chloroplasts of "Calcifying Isochrysidales", resulting in apparent resilience relative to other groups in this study.

Discussion

Overall our method has demonstrated a good degree of accuracy when it comes to making classifications of cell types into ecologically relevant groups. The groups that consistently had the greatest accuracy were "Calcifying Isochrysidales", "Coccolithophores", and "Picophytoplankton"; all of which maintained more than 85% accuracy across the random forest predictions (both key group and all group libraries). The inclusion of the suspected "nano-phytoflagellate" groups did cause some

overall reduction in the accuracy of the technique, from ~90% to 70%, but given that we have just two variables to make predictions (charge at t_{50} and effective radius), this is something that we anticipate can be improved if the technique was adjusted to capture additional predictor variables. The findings of the susceptibility library assessment also demonstrate that following size normalisation there must be some underlying biological feature that is enhancing the strong classification ability of some of the groups, notably "Calcifying Isochrysidales" and "Eustigmatales", and thus this presents an important avenue for further investigative studies into the potential mechanistic underpinnings.

Current applicability of the method and recommendations

Whilst we demonstrate the ability of our technique to classify nanophytoplankton into groups of relevance, it is critical that the method can quantify the abundance of different groups in natural seawater samples. This will require field testing alongside more traditional techniques *e.g.* microscope taxonomy and cytometry to validate the applicability of using a predefined susceptibility library based on a limited selection of 52 monocultures. Methodological and engineering advancements will need to be made to take this method to such a stage. As things stand, in obtaining the susceptibility measurements presented here, samples of an uncontrolled volume were drop cast following concentration by centrifugation and left to settle on the electrode beforehand (Kumar et al. 2020). Therefore, given the uncertainties around the volume of sample used, it was not possible to quantify abundance of the samples measured. A prototype instrument that implements the fluoro-electrochemical technique with a flow cell type system could help to overcome this issue, as both sample volume and flow rate could be quantifiable and controllable. Not only could this make the laboratory-based measurements higher throughput (akin to a FlowCam, for example), it would also be an essential step towards the long-term goal of the technique being used on autonomous platforms, whereby the collection of *in situ* spatio-temporal data of nanophytoplankton community structure would be invaluable to monitoring the effects of environmental change.

As mentioned previously, devices such as FlowCam and Imaging FlowCytobot use combinations of flow cytometry fluorescence measurements with rapid imaging of cells. Whilst highly progressive in helping us to understand planktonic communities, they fall short in their ability to distinguish at the much smaller size ranges – especially when many cell types in the nanophytopankton range can have a similar apparent morphology and size. Understandably, there is a consequent trade-off between magnification, image quality, and the size range of phytoplankton being measured. This is likely to make any machine learning algorithms poorer at the lower limits of the nanophytoplankton size range. The key novelty of our classifying technique at the nanophytoplankton level is the extra tool for distinguishing phytoplankton cell types that has not been previously applied: the electrochemical

susceptibility of the chlorophyll *a* fluorescence signal. We can get a good degree of categorisation overall from simply combining the charge at t_{50} value with a simple effective radius estimate. We also demonstrate that our design has potential to distinguish picophytoplankton, as well as larger nanophytoplankton, spanning three orders of magnitude. Given the relatively simple optics set-up of our technique, compared to others, it is also likely to be more affordable, thus making it potentially more appealing for widespread use in conjunction with autonomous platforms.

It was evident from our assessment that some groups were more easily predicted than others. Of the key functional groups, our technique currently falls short when it comes to distinguishing diatoms (~60% accuracy, see Table 2), and of the other groups, the lowest accuracy was in predicting "Non-calcifying Isochrysidales" and "Green algae" (~32 and ~31%, respectively, see Table 2). Therefore, due to the differing levels of classification accuracy across the groups as things stand, it is likely the set-up would yield more promising *in situ* measurements from nanophytoplankton communities dominated by taxa belonging to the more easily classifiable groups presented here. To advance our method further, and with minimal increase in cost, a couple of adjustments to both the apparatus and method could give us additional variables that will likely improve predictive ability. Firstly, with the addition of more excitation and emission pathways, a measurement of secondary chlorophyll *b* pigment fluorescence could be obtained. In marine phytoplankton, this pigment is unique to chlorophytes (or green algae). In the nanophytoplankton range, a large degree of confusion for our method was between the "Diatoms" and "Green algae", and therefore this addition would help to reduce this. Such an advancement could also assist at the picophytoplankton scale, where the majority of pico-eukaryotes are either prasinophytes containing chlorophyll *b*, or cyanobacteria containing phycocyanin (a chlorophyll accessory pigment, also with distinguishable autofluorescence properties).

Secondly, where there is overlap between calcified cell groups and others, we might be able to use the intrinsic dissolution of the calcite during the electrochemical experiments to observe changes in the apparent radius before and after the experiment. In brief, the electrochemical oxidation of water means that H^+ is generated in the vicinity of the electrode, decreasing the pH around the cells. Consequently, it has been observed that during the short timespan of the experimental measurements presented here, the smaller extracellular calcite coccospheres (*e.g. E. huxleyi*) can be completely dissolved, such that a before and after measure of cell radius could indicate the calcification of a cell. Previous work has demonstrated that such a method can also be applied to estimate the mass of extra-cellular calcium carbonate of entire coccospheres (Yang et al. 2022; Fan et al. 2022), which is another relevant measurement for understanding marine biogeochemical cycles, notably the 'rain ratio' (Hutchins 2011). Having an additional predictor variable of the ratio of cellular radius before and after the fluoro-electrochemical experiment would thereby provide an entirely affordable and achievable additional dimension for improved cell categorisation in the random forest algorithms, as well as generating an estimate of cellular calcite which could be of great value to ocean biogeochemists.

Lastly, there is potential for more sophisticated artificial intelligence (or machine learning) based approaches for developing the predictive ability of our technique that take advantage of the full range of data that is harvested from the experiments presented here. In terms of the chlorophyll *a* measurement, we only use a single parameter derived from each transient profile: charge at t_{50}. If the full transient profiles were to be assessed then it is likely this could improve the predictive power of the susceptibility library. Indeed, the shape of the transients appear to be idiosyncratic at a group-specific level (see Figure S2, SI). Likewise, in terms of the bright-field imaging, we only make a relatively crude interpretation of the cell radius. Whilst useful for the basic analytics of the assessment presented here, there is scope that finer details of the images of each group could be categorised in some kind of machine learning algorithm, as has been demonstrated for images acquired by FlowCAM (Camoying and Yñiguez 2016). Thus, with the two lines of data acquisition for the predictor variables presented in this study, along with the minor methodological tweaks suggested above to generate more predictor variables, a more sophisticated AI based technique that combines all of these aspects will likely give a better degree of accuracy across more of the relevant groups.

Summary

We have presented a novel fluoro-electrochemical technique for classifying marine nanophytoplankton, and critically assessed this by testing its ability to predict phytoplankton groupings from two simple parameters: charge required to reduce per cell chlorophyll *a* fluorescence by 50% and effective cell radius. This returned an excellent degree of accuracy when only considering taxa belonging to key functional groups (37 strains), but a reduced degree of accuracy when a broader range of groups, encompassing likely "nano-phytoflagellates", were considered (52 strains). We demonstrate that the technique relies on the general positive size scaling of the susceptibility across the groups to provide additional distinguishing power, and when size is normalised for there are some groups that demonstrate exceptional resilience to the highly oxidative conditions of our technique, notably "Calcifying Isochrysidales". This presents an avenue for further investigation into the biological underpinnings of this new method. Whilst the technique currently has its limitations as we report, with advancement of the set-up to make complimentary measurements, the predictive power of the method could be enhanced. Critically, if the technique is to eventually be used for real world *in situ* measurements, the next step of assessment is to test its ability in quantifying abundance of different groupings in natural samples alongside more traditional techniques. If such further testing yields positive results, we anticipate that our technique could be adapted to work in conjunction with autonomous platforms, with the potential to greatly enhance our ability in monitoring nanophytoplankton community structure.

642 **Author Contributions**

643 S.B., M.Y., C.B.-M., R.G.C., H.A.B., and R.E.M.R. conceptualized the study; S.B. (phytoplankton),
644 M.Y., and C.B.-M (electrochemistry), contributed to the methodology; S.B. conducted the experiments;
645 S.B. and M.Y., analysed the data, S.B. wrote the manuscript, M.Y., H.C., C.B.-M., R.G.C., H.A.B., and
646 R.E.M.R., reviewed and edited the manuscript.

647 **Acknowledgements**

648 This research was conducted with the support from the Oxford Martin School Programme on
649 Monitoring Ocean Ecosystems

650

651 **References**

652 Álvarez, E., M. Moyano, Á. López-Urrutia, E. Nogueira, and R. Scharek. 2014. Routine
653 determination of plankton community composition and size structure: A comparison between
654 FlowCAM and light microscopy. J Plankton Res **36**: 170–184. doi:10.1093/plankt/fbt069

655 Alves-De-Souza, C., T. S. Benevides, J. B. O. Santos, P. von Dassow, L. Guillou, and M. Menezes.
656 2017. Does environmental heterogeneity explain temporal β diversity of small eukaryotic
657 phytoplankton? Example from a tropical eutrophic coastal lagoon. J Plankton Res **39**: 698–714.
658 doi:10.1093/plankt/fbx026

659 Anderson, S. I., A. D. Barton, S. Clayton, S. Dutkiewicz, and T. A. Rynearson. 2021. Marine
660 phytoplankton functional types exhibit diverse responses to thermal change. Nat Commun **12**.
661 doi:10.1038/s41467-021-26651-8

662 Anderson, T. R. 2005. Plankton functional type modelling: Running before we can walk? J Plankton
663 Res **27**: 1073–1081. doi:10.1093/plankt/fbi076

664 Balzano, S., D. Marie, P. Gourvil, and D. Vaulot. 2012. Composition of the summer photosynthetic
665 pico and nanoplankton communities in the Beaufort Sea assessed by T-RFLP and sequences of
666 the 18S rRNA gene from flow cytometry sorted samples. ISME Journal **6**: 1480–1498.
667 doi:10.1038/ismej.2011.213

668 Barnes, M. K., G. H. Tilstone, D. J. Suggett, C. E. Widdicombe, J. Bruun, V. Martinez-Vicente, and
669 T. J. Smyth. 2015. Temporal variability in total, micro- and nano-phytoplankton primary
670 production at a coastal site in the Western English Channel. Prog Oceanogr **137**: 470–483.
671 doi:10.1016/j.pocean.2015.04.017

672 Bendif, E. M., I. Probert, O. A. Archontikis, J. R. Young, L. Beaufort, R. E. Rickaby, and D. Filatov.
673 2023. Rapid diversification underlying the global dominance of a cosmopolitan phytoplankton.
674 ISME J. doi:10.1038/s41396-023-01365-5

675 Bestion, E., S. Barton, F. C. García, R. Warfield, and G. Yvon-Durocher. 2020. Abrupt declines in
676 marine phytoplankton production driven by warming and biodiversity loss in a microcosm
677 experiment. Ecol Lett **23**: 457–466. doi:10.1111/ele.13444

678 Bestion, E., B. Haegeman, S. Alvarez Codesal, A. Garreau, M. Huet, S. Barton, and J. M. Montoya.
679 2021. Phytoplankton biodiversity is more important for ecosystem functioning in highly variable

thermal environments. Proceedings of the National Academy of Sciences **118**. doi:10.1073/pnas.2019591118/-/DCSupplemental

Bolaños, L. M., L. Karp-Boss, C. J. Choi, and others. 2020. Small phytoplankton dominate western North Atlantic biomass. ISME Journal **14**: 1663–1674. doi:10.1038/s41396-020-0636-0

Breiman, L. 2001. Random Forests. Mach Learn **45**: 5–32.

Camoying, M. G., and A. T. Yñiguez. 2016. FlowCAM optimization: Attaining good quality images for higher taxonomic classification resolution of natural phytoplankton samples. Limnol Oceanogr Methods **14**: 305–314. doi:10.1002/lom3.10090

Dugenne, M., M. Thyssen, D. Nerini, C. Mante, J. C. Poggiale, N. Garcia, F. Garcia, and G. J. Grégori. 2014. Consequence of a sudden wind event on the dynamics of a coastal phytoplankton community: An insight into specific population growth rates using a single cell high frequency approach. Front Microbiol **5**. doi:10.3389/fmicb.2014.00485

Fan, X., C. Batchelor-McAuley, M. Yang, S. Barton, R. E. M. Rickaby, H. A. Bouman, and R. G. Compton. 2022. Quantifying the Extent of Calcification of a Coccolithophore Using a Coulter Counter. Anal Chem **94**: 12664–12672. doi:10.1021/acs.analchem.2c01971

Finkel, Z. v., J. Beardall, K. J. Flynn, A. Quigg, T. A. v. Rees, and J. A. Raven. 2010. Phytoplankton in a changing world: Cell size and elemental stoichiometry. J Plankton Res **32**: 119–137. doi:10.1093/plankt/fbp098

Fragoso, G. M., A. J. Poulton, N. J. Pratt, G. Johnsen, and D. A. Purdie. 2019. Trait-based analysis of subpolar North Atlantic phytoplankton and plastidic ciliate communities using automated flow cytometer. Limnol Oceanogr **64**: 1763–1778. doi:10.1002/lno.11189

Fujiwara, S., M. Tsuzuki, M. Kawachi, and N. Minaka. 2001. MOLECULAR PHYLOGENY OF THE HAPTOPHYTA BASED ON THE rbc L GENE AND SEQUENCE VARIATION IN THE SPACER REGION OF THE RUBISCO OPERON 1. J Phycol **37**: 121–129.

Green, J., P. Course, and G. Tarran. 1996. The life-cycle of Emiliania huxleyi: A brief review and a study of relative ploidy levels analysed by flow cytometry. Journal of Marine Systems **9**: 33–44.

Hutchins, D. A. ,. 2011. Forecasting the rain ratio. Nature **476**: 41–42.

Kumar, A. K. S., Y. Zhang, D. Li, and R. G. Compton. 2020. A mini-review: How reliable is the drop casting technique? Electrochem commun **121**. doi:10.1016/j.elecom.2020.106867

Leblanc, K., B. Quéguiner, F. Diaz, and others. 2018. Nanoplanktonic diatoms are globally overlooked but play a role in spring blooms and carbon export. Nat Commun **9**. doi:10.1038/s41467-018-03376-9

Litchman, E., and C. A. Klausmeier. 2008. Trait-based community ecology of phytoplankton. Annu Rev Ecol Evol Syst **39**: 615–639. doi:10.1146/annurev.ecolsys.39.110707.173549

López-Sandoval, D. C., T. Rodríguez-Ramos, P. Cermeño, C. Sobrino, and E. Marañón. 2014. Photosynthesis and respiration in marine phytoplankton: Relationship with cell size, taxonomic affiliation, and growth phase. J Exp Mar Biol Ecol **457**: 151–159. doi:10.1016/j.jembe.2014.04.013

Marañón, E., P. Cermeño, D. C. López-Sandoval, T. Rodríguez-Ramos, C. Sobrino, M. Huete-Ortega, J. M. Blanco, and J. Rodríguez. 2013. Unimodal size scaling of phytoplankton growth and the size dependence of nutrient uptake and use. Ecol Lett **16**: 371–379. doi:10.1111/ele.12052

Morel, F. M. M., J. G. Rueter, D. M. Anderson, and R. R. L. Guillard. 1979. AQUIL: A CHEMICALLY DEFINED PHYTOPLANKTON CULTURE MEDIUM FOR TRACE METAL STUDIES 1 2 . J Phycol **15**: 135–141. doi:10.1111/j.1529-8817.1979.tb02976.x

Nair, A., S. Sathyendranath, T. Platt, J. Morales, V. Stuart, M. H. Forget, E. Devred, and H. Bouman. 2008. Remote sensing of phytoplankton functional types. Remote Sens Environ **112**: 3366–3375. doi:10.1016/j.rse.2008.01.021

Olson, R. J., and H. M. Sosik. 2007. A submersible imaging-in-flow instrument to analyze nano-and microplankton: Imaging FlowCytobot. Limnol Oceanogr Methods **5**: 195–203. doi:10.4319/lom.2007.5.195

Pinckney, J. L., C. R. Benitez-Nelson, R. C. Thunell, F. Muller-Karger, L. Lorenzoni, L. Troccoli, and R. Varela. 2015. Phytoplankton community structure and depth distribution changes in the Cariaco Basin between 1996 and 2010. Deep Sea Res 1 Oceanogr Res Pap **101**: 27–37. doi:10.1016/j.dsr.2015.03.004

Piwosz, K. 2019. Weekly dynamics of abundance and size structure of specific nanophytoplankton lineages in coastal waters (Baltic Sea). Limnol Oceanogr **64**: 2172–2186. doi:10.1002/lno.11177

Snoeijs, P., S. Busse, and M. Potapova. 2002. The importance of diatom cell size in community analysis. J Phycol **38**: 265–281. doi:10.1046/j.1529-8817.2002.01105.x

Sosik, H. M., and R. J. Olson. 2007. Automated taxonomic classification of phytoplankton sampled with imaging-in-flow cytometry. Limnol Oceanogr Methods **5**: 204–216. doi:10.4319/lom.2007.5.204

Stern, R., K. Picard, J. Clarke, and others. 2023. Composition and Patterns of Taxa Assemblages in the Western Channel Assessed by 18S Sequencing, Microscopy and Flow Cytometry. J Mar Sci Eng **11**: 480. doi:10.3390/jmse11030480

Tarran, G. A., and J. T. Bruun. 2015. Nanoplankton and picoplankton in the Western English Channel: Abundance and seasonality from 2007-2013. Prog Oceanogr **137**: 446–455. doi:10.1016/j.pocean.2015.04.024

Tarran, G. A., J. L. Heywood, and M. v. Zubkov. 2006. Latitudinal changes in the standing stocks of nano- and picoeukaryotic phytoplankton in the Atlantic Ocean. Deep Sea Res 2 Top Stud Oceanogr **53**: 1516–1529. doi:10.1016/j.dsr2.2006.05.004

de Vargas, C., S. Audic, N. Henry, and others. 2015. Eukaryotic plankton diversity in the sunlit ocean. Science (1979) **348**.

Ward, B. A., E. Marañón, B. Sauterey, J. Rault, and D. Claessen. 2017. The size dependence of phytoplankton growth rates: A trade-off between nutrient uptake and metabolism. American Naturalist **189**: 170–177. doi:10.1086/689992

Widdicombe, C. E., D. Eloire, D. Harbour, R. P. Harris, and P. J. Somerfield. 2010. Long-term phytoplankton community dynamics in the Western English Channel. J Plankton Res **32**: 643–655. doi:10.1093/plankt/fbp127

Yang, M., C. Batchelor-McAuley, S. Barton, R. E. M. Rickaby, H. A. Bouman, and R. G. Compton. 2022. Single-entity coccolithophore electrochemistry shows size is no guide to the degree of calcification. Environmental Science: Advances **1**: 156–163. doi:10.1039/d2va00025c

Yang, M., C. Batchelor-Mcauley, L. Chen, Y. Guo, Q. Zhang, R. E. M. Rickaby, H. A. Bouman, and R. G. Compton. 2019. Fluoro-electrochemical microscopy reveals group specific differential

susceptibility of phytoplankton towards oxidative damage. Chem Sci **10**: 7988–7993. doi:10.1039/c9sc02699a

Young, J., M. Geisen, L. Cros, A. Kleijne, C. Sprengel, I. Probert, and J. Østergaard. 2003. A guide to extant coccolithophore taxonomy.

Yu, J., M. Yang, C. Batchelor-McAuley, S. Barton, R. E. M. Rickaby, H. A. Bouman, and R. G. Compton. 2022. Rapid Opto-electrochemical Differentiation of Marine Phytoplankton. ACS Measurement Science Au **2**: 342–350. doi:10.1021/acsmeasuresciau.2c00017

Yu, J., M. Yang, C. Batchelor-McAuley, S. Barton, R. E. M. Rickaby, H. A. Bouman, and R. G. Compton. 2023. Does the life cycle stage matter for distinguishing phytoplankton via fluoro-electrochemical microscopy? Cell Rep Phys Sci **4**. doi:10.1016/j.xcrp.2022.101223

Supplemental Information for:

A novel fluoro-electrochemical technique for classifying diverse marine nanophytoplankton

Samuel Barton[1*], Minjun Yang[2], Haotian Chen[2], Christopher Batchelor-McAuley[2, 3], Richard G. Compton[2], Heather A. Bouman[1], Rosalind E.M. Rickaby[1]

[1] Department of Earth Sciences, University of Oxford, South Parks Road, Oxford, OX1 3AN, UK

[2] Physical and Theoretical Chemistry Laboratory, Department of Chemistry, University of Oxford, South Parks Road, Oxford, OX1 3QZ, UK

[3] School of Chemistry, Trinity College Dublin, Dublin 2, Ireland

* Corresponding author: samuel.barton@earth.ox.ac.uk

Number of Figures: 10

Number of Tables: 16

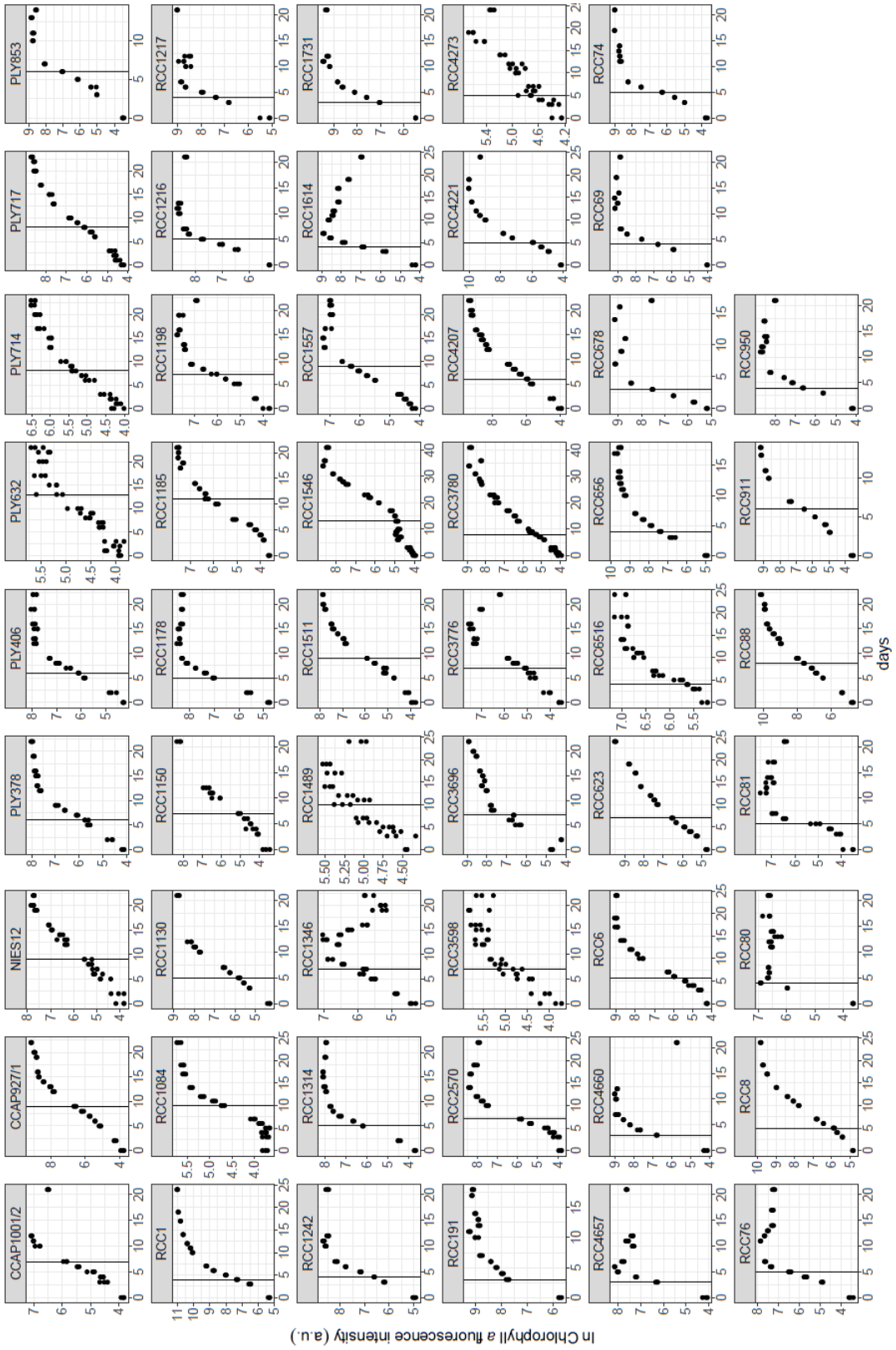

Figure S1: Culture growth curves for each of the strains in Table S1, as natural log transformed Chlorophyll *a* fluorescence intensity against days. The data points represent technical replicated measurements for each culture on each day. The vertical black line corresponds to the time-point when the electrochemical measurements were made, as described in the main text.

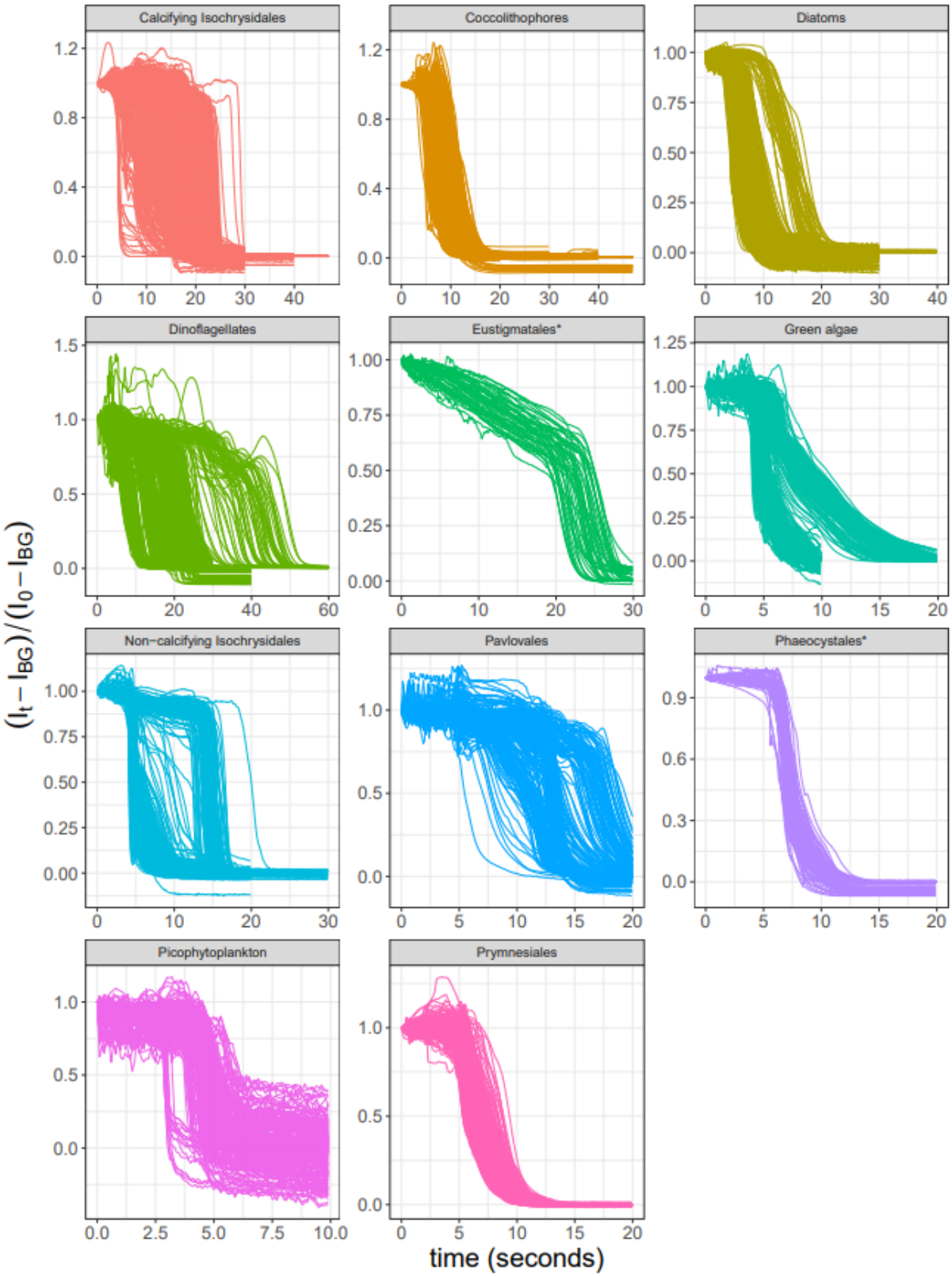

Figure S2: Normalised Chlorophyll *a* fluorescence transients for each of the relevant phytoplankton groups in this study. Each line represents a single cell measurement (4884 individual cell measurements in total, across the groups). *denotes groups that were just represented by a single species (see Table S3).

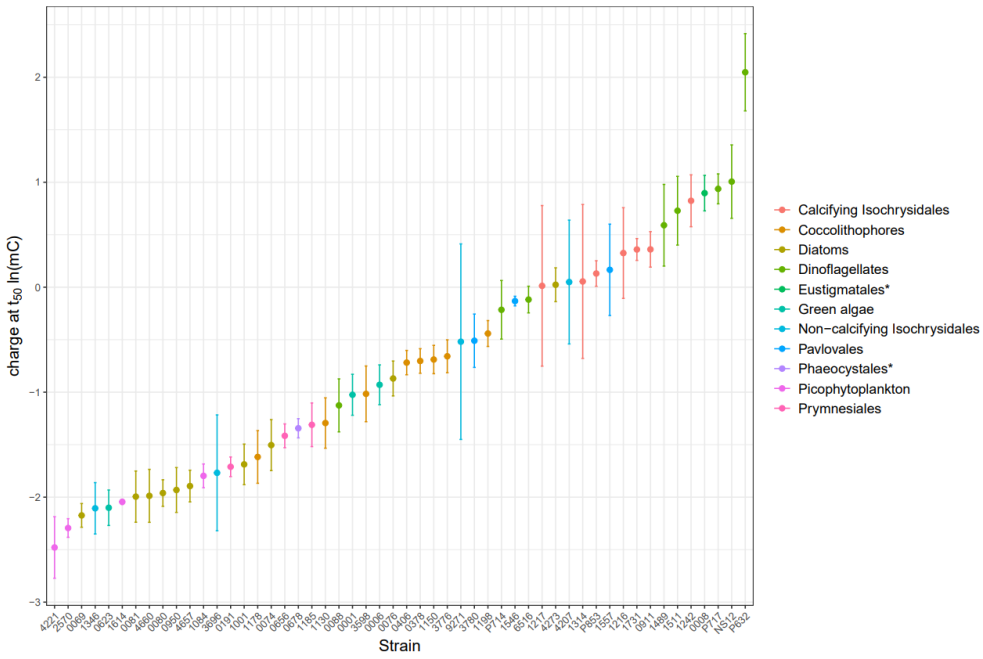

Figure S3: Natural log mean charge at t_{50} (mC) for each of the strains measured with the electrochemical chlorophyll *a* quenching method in this study. Data points represent the mean for each strain, and error bars represent the standard deviation of the mean (see Tables S3 and S5). Colour coding represents the grouping that each strain is assigned to.

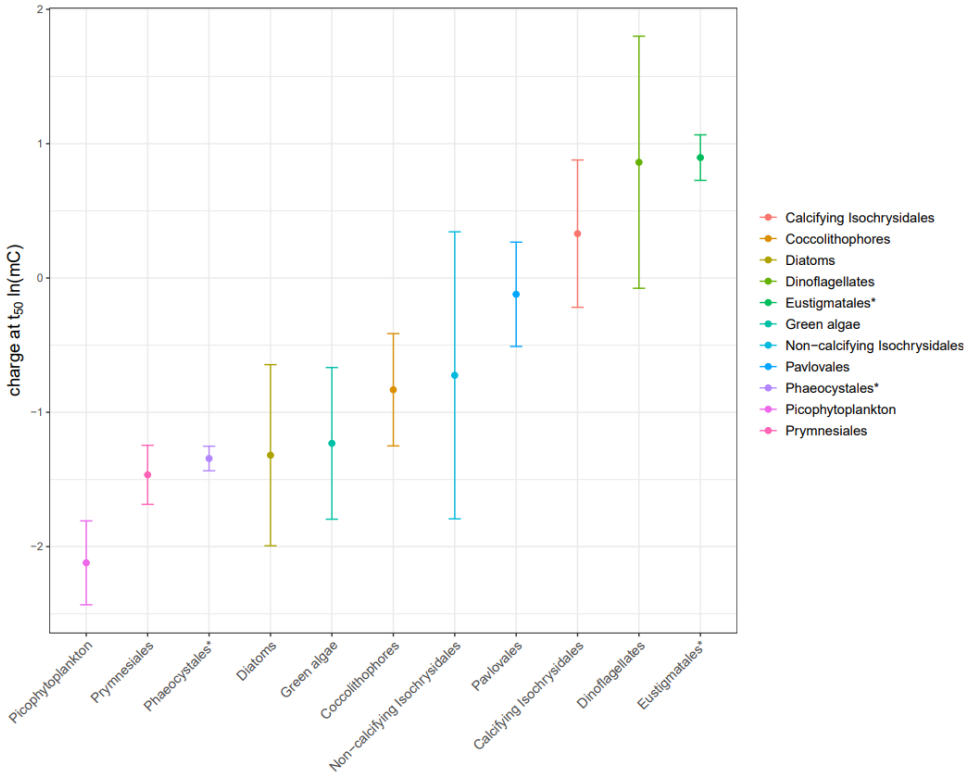

Figure S4: Natural log mean charge at t_{50} (mC) at the level of each phytoplankton grouping defined in this study. Data points represent the mean for each strain, and error bars represent the standard deviation of the mean (see Tables S4 and S6). Colour coding represents the grouping that each strain is assigned to.

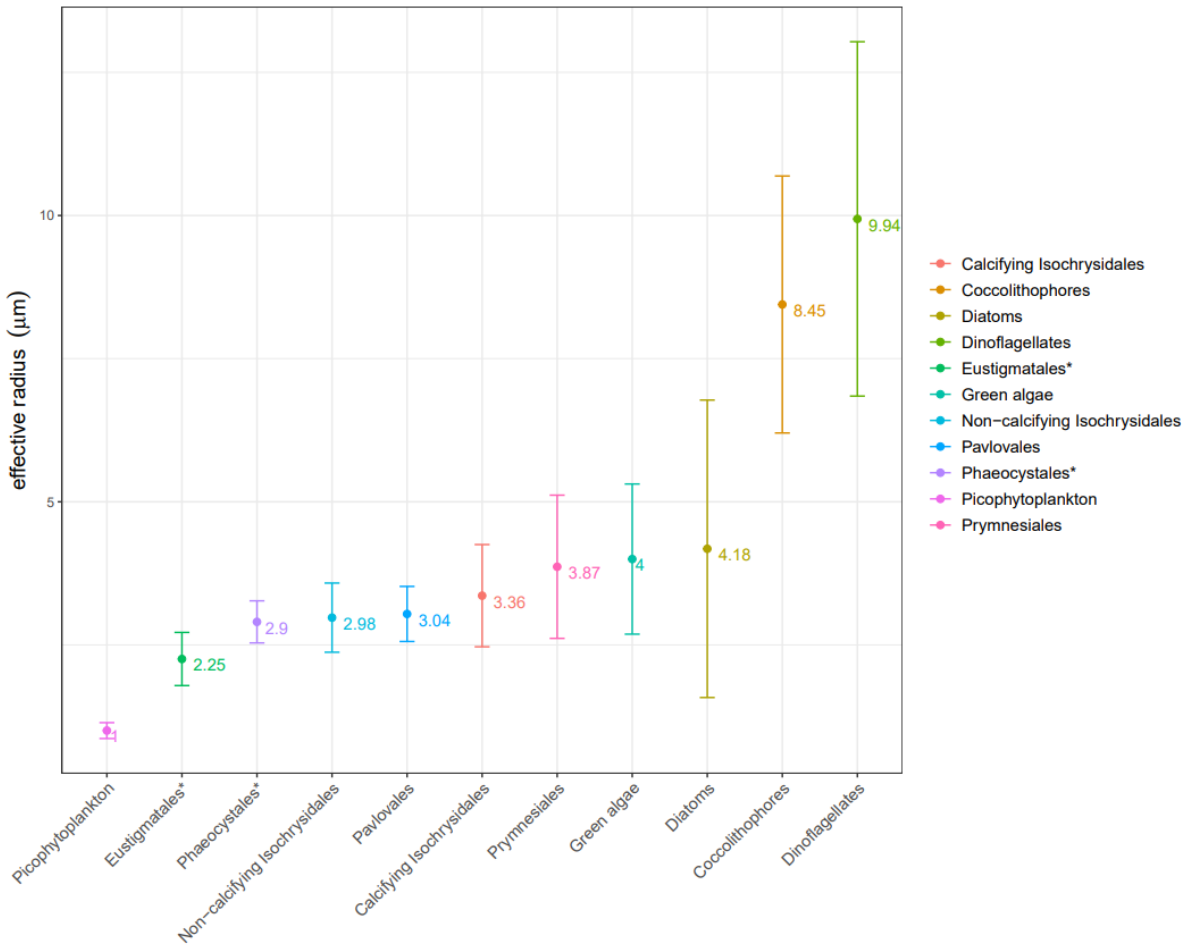

Figure S5: Mean effective radius (µm) at the level of each phytoplankton grouping defined in this study. Data points represent the mean for each strain, and error bars represent the standard deviation of the mean (see Tables S4 and S6). The numbers alongside respective datapoints are the mean effective radius p in µm. Colour coding represents the grouping that each strain is assigned to.

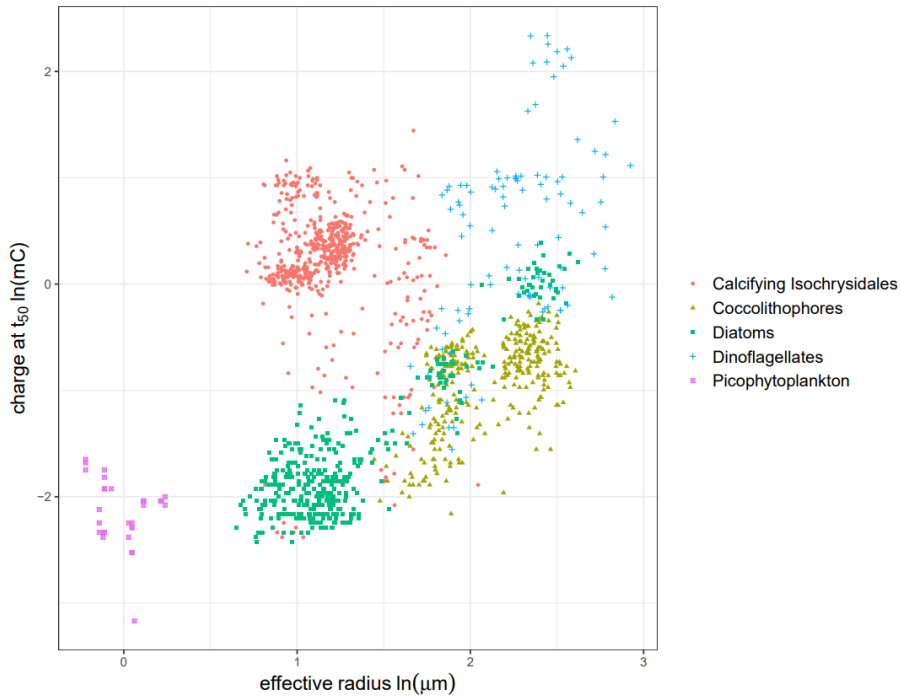

Figure S6: A scatterplot of natural log charge at t_{50} (mC) against natural log effective cell radius (µm) for the 'key functional groups' of cells measured in this study, using the balanced dataset (*n* = 1406, see Table S4 for a summary of the data presented here). The random forest analysis on this dataset returned an overall accuracy of 91.5% with the training data and 90.6% with the testing (see Tables 1 and S9).

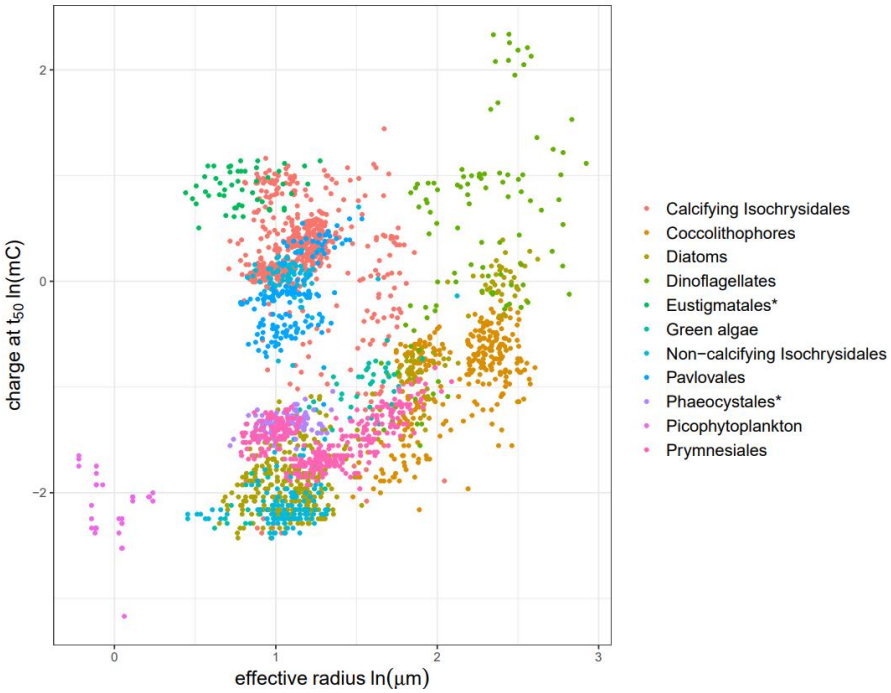

Figure S7: A scatterplot of natural log charge at t_{50} (mC) against natural log effective cell radius (µm) for all groups of cells measured in this study, with the balanced dataset (*n* = 2277, see Table S4 for a summary of the data presented here). The random forest analysis on this dataset returned an overall accuracy of 69.1% with the training data and 71.7% with the testing (see Tables 2 and S12).*denotes groups that were just represented by a single species.

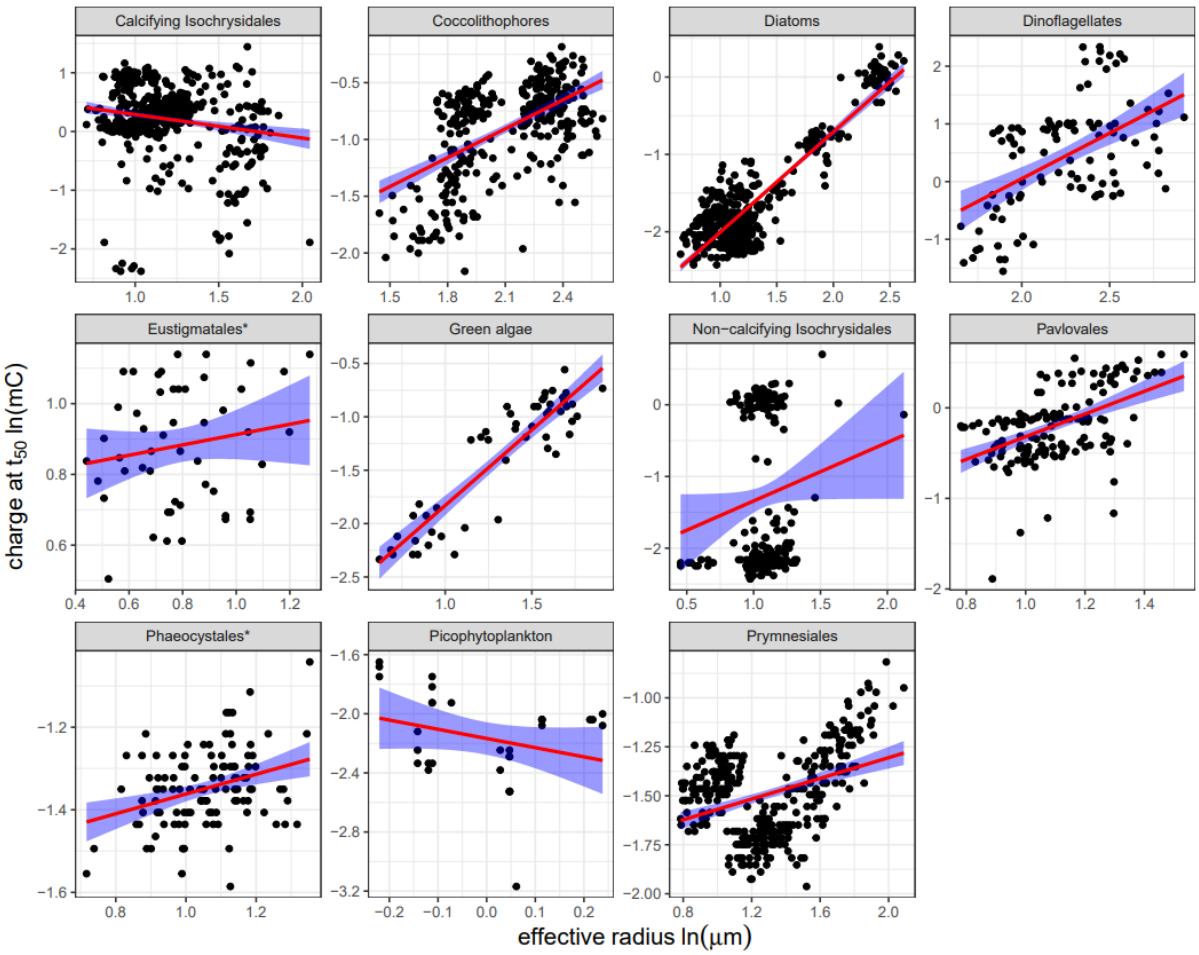

Figure S8: Scatterplots of natural log charge at t_{50} (mC) against natural log effective cell radius (µm) of cells measured for each phytoplankton group in this study, following the balancing of strain representation per group (*n* = 2277). The red line indicates the overall slope of the allometric relationship modelled for each level of grouping, and the blue shading is a visual representation of the 95% confidence of this fit. See Tables S14 for the coefficients of each individual model fit, and respective *p* values. *denotes groups that were just represented by a single species.

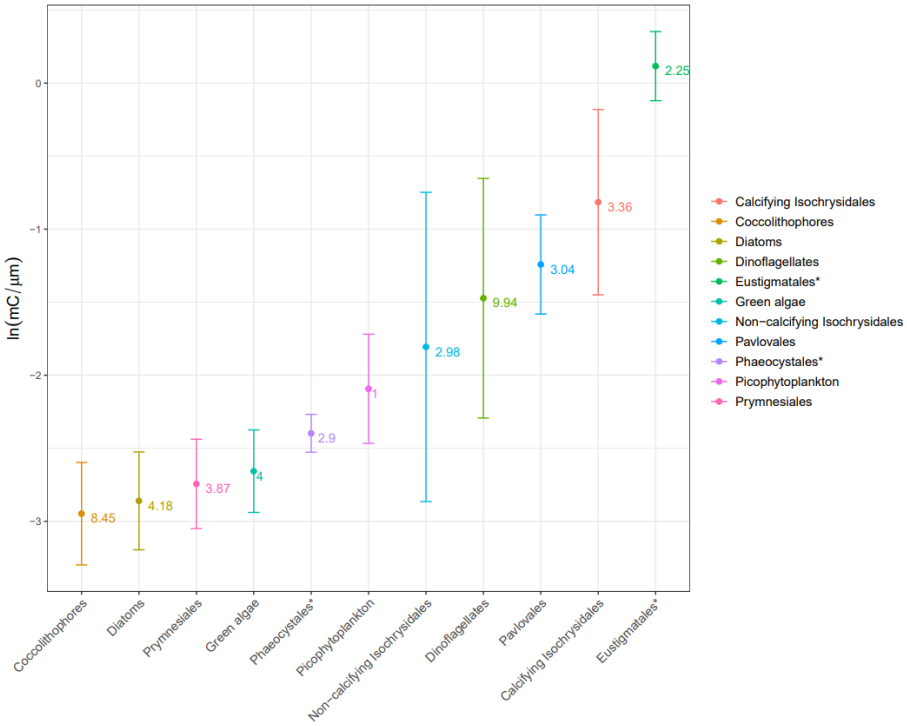

Figure 9: Comparison of per group natural log transformed mean of size normalised charge at t_{50}. Data points represent the mean value for each group and the error bars are for standard deviation, following balancing the representation of the individual strains within each group. The labelled numbers alongside the data points represent the mean effective radius for each of the groups.

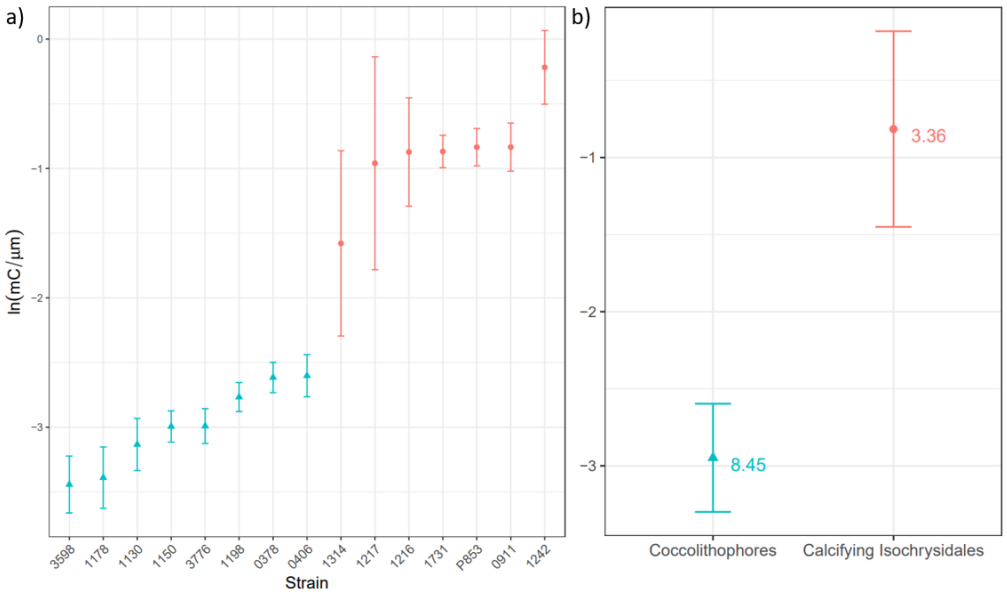

Figure S10: **(a)** Comparison of natural log size normalised charge at t_{50} across the different strains of "Coccolithophore" (blue) and "Calcifying Isochrysidales" (red) **(b)** Comparison of natural log size normalised mean charge at t_{50} the group level for "Coccolithophores" and "Calcifying Isochrysidales". Data points represent the mean values and the error bars are for standard deviation. The labelled numbers alongside the data points represent the mean effective radius. These plots clearly demonstrate that despite their much smaller size, "Calcifying Isochrysidales" are significantly more resilient in terms of their chlorophyll *a* "switch-off".

Table S1: A list of all the 52 strains used in this study, including their grouping (in this study), their culture collection strain numbers, and their respective growth medium enrichment (see Table S2). Strain prefixes relate to the respective culture collections where the strain was obtained (RCC = Roscoff Culture Collection (Roscoff, France), CCAP = Culture Collection of Algae and Protozoa (Oban, UK), and PLY = The Marine Biological Association (Plymouth, UK)

Group	Species detail	Strain	Synethetic seawater based growth medium
Calcifying Isochrysidales	*Emiliania huxleyi,* non-calcified haploid	RCC 1217	K/2
Calcifying Isochrysidales	*Emiliania huxleyi,* morphotype A,light -moderately calcified	RCC 911	K/2
Calcifying Isochrysidales	*Emiliania huxleyi,* morphotype A, moderately calcified	RCC 1731	K/2
Calcifying Isochrysidales	*Emiliania huxleyi,* morphotype A/R, over-calcified with bulkycentre	PLY 853	K/2
Calcifying Isochrysidales	*Emiliania huxleyi* morphotype A/R, over-calcified shields	RCC 1216	K/2
Calcifying Isochrysidales	*Emiliania huxleyi,* non-calcified diploid	RCC 1242	K/2
Calcifying Isochrysidales	*Gephyrocapsa oceanica*	RCC 1314	K/2
Coccolithophores	*Calcidiscus leptoporus* (1)	RCC 1130	K/2
Coccolithophores	*Calcidiscus leptoporus* (2)	RCC 1150	K/2
Coccolithophores	*Calyptrosphaera sphaeroidea*	RCC 1178	K/2
Coccolithophores	*Chrysotila dentata* (1)	PLY 378	K/2
Coccolithophores	*Chrysotila dentata* (2)	PLY 406	K/2
Coccolithophores	*Coccolithus braarudii*	RCC 1198	K/2
Coccolithophores	*Coccolithus pelagicus*	RCC 3776	K/2
Coccolithophores	*Scyphosphaera apsteinii*	RCC 3598	L1
Diatoms	*Nitzchia closterium*	RCC 81	K
Diatoms	*Nitzchia* sp.	RCC 80	K
Diatoms	*Phaeodactylum tricornutum*	RCC 69	K
Diatoms	*Coscinodiscus* sp.	RCC 4273	K
Diatoms	*Halamphora coffeaeformis*	CCAP 1001/2	K
Diatoms	*Minidiscus comicus*	RCC 4660	K
Diatoms	*Minidiscus variabilis*	RCC 4657	K
Diatoms	*Skeletonema japonicum*	RCC 74	K
Diatoms	*Thalassiosira pseudonana*	RCC 950	K
Diatoms	*Thalassiosira weissflogii*	RCC 76	K
Dinoflagellates	*Amphidinium carterae*	RCC 88	F/2
Dinoflagellates	*Karenia papilionacea*	RCC 6516	K
Dinoflagellates	*Lepidodinium chlorophorum*	RCC 1489	F/2
Dinoflagellates	*Heterocapsa triquetra*	PLY 717	F/2
Dinoflagellates	*Prorocentrum micans*	NIES-12	F/2
Dinoflagellates	*Prorocentrum minimum*	PLY 714	F/2
Dinoflagellates	*Scripsiella trochoidea*	PLY 632	F/2
Dinoflagellates	*Thoracosphaera heimii*	RCC 1511	K/2
Eustigmatales*	*Nannochloropsis granulata*	RCC 8	F/2
Green algae	*Chlamydomonas concordia*	RCC 1	F/2
Green algae	*Dunaliella tertiolecta*	RCC 6	K
Green algae	*Bigelowiella natans*	RCC 623	F/2
Non-calcifying Isochrysidales	*Isochrysis galbana*	CCAP 927/1	K
Non-calcifying Isochrysidales	*Isochrysis litoralis*	RCC 1346	F/2

Non-calcifying Isochrysidales	*Isochrysis* sp.	RCC 4207	K
Non-calcifying Isochrysidales	*Ruttnera* sp.	RCC 3696	F/2
Pavlovales	*Diacronema vlkianum* (1)	RCC 1546	F/2
Pavlovales	*Diacronema vlkianum* (2)	RCC 3780	F/2
Pavlovales	*Pavlova granifera*	RCC 1557	F/2
Phaeocystales*	*Phaeocystis globosa*	RCC 678	K
Picophytoplankton	*Micromonas pusilla*	RCC 1614	K
Picophytoplankton	*Osteococcus tauri*	RCC 4221	F/2
Picophytoplankton	*Synechococcus* sp. (1)	RCC 1084	F/2
Picophytoplankton	*Synechococcus* sp. (2)	RCC 2570	F/2
Prymnesiales	*Chrysochromulina camella*	RCC 1185	K/2
Prymnesiales	*Chrysochromulina* sp.	RCC 656	K
Prymnesiales	*Prymnesium parvum*	RCC 191	K

Table S2: The final concentration of the components of Aquil Synethetic Ocean Water (Morel et al. 1979), used to make all of the culture growth mediums (See Table S1). For medium enrichment applied to each see the following references: K (Keller et al. 1987), F/2 (Guillard and Ryther 1962), L1 (Guillard and Hargraves 1993).

		Molar Concentration in final SOW based medias (mol dm^{-3})
Synthetic Ocean Water (SOW) based on the Aquil medium recipe	NaCl	4.20×10^{-1}
	Na_2SO_4	2.88×10^{-2}
	KCl	9.39×10^{-3}
	$NaHCO_3$	2.38×10^{-3}
	KBr	8.40×10^{-4}
	H_3BO_3	4.85×10^{-5}
	NaF	7.15×10^{-5}
	$MgCl_2.6H_2O$	5.46×10^{-2}
	$CaCl_2.2H_2O$	1.05×10^{-2}
	$SrCl_2.6H_2O$	6.38×10^{-5}

Table S3. A summary of the predictor variables derived at the strain level, with the unbalanced dataset (i.e. variable *n* across the strains within each group).

Group	Species detail	Strain	*n*	t_{50} (s)	SD t_{50}	Charge at t_{50} (mC)	SD Charge at t50	effective radius (µm)	SD effective radius
Calcifying Isochrysidales	*Emiliania huxleyi,* non-calcified haploid	RCC 1217	115	13.60	3.82	1.00	0.42	2.76	0.59
Calcifying Isochrysidales	*Emiliania huxleyi,* morphotype A,light - moderately calcified	RCC 911	198	16.92	1.40	1.44	0.25	3.31	0.33
Calcifying Isochrysidales	*Emiliania huxleyi,* morphotype A, moderately calcified	RCC 1731	311	16.94	0.93	1.44	0.17	3.44	0.32
Calcifying Isochrysidales	*Emiliania huxleyi,* morphotype A/R, over-calcified with bulkycentre	PLY 853	158	14.97	0.91	1.12	0.14	2.64	0.22
Calcifying Isochrysidales	*Emiliania huxleyi* morphotype A/R, over-calcified shields	RCC 1216	277	16.74	2.81	1.44	0.42	3.35	0.23
Calcifying Isochrysidales	*Emiliania huxleyi,* non-calcified diploid	RCC 1242	80	21.21	2.44	2.28	0.49	2.90	0.52

Calcifying Isochrysidales	*Gephyrocapsa oceanica*	RCC 1314	132	13.65	4.98	1.05	0.78	5.12	0.52
Coccolithophores	*Calcidiscus leptoporus* (1)	RCC 1130	111	7.21	0.81	0.26	0.06	6.26	0.56
Coccolithophores	*Calcidiscus leptoporus* (2)	RCC 1150	55	10.08	0.68	0.51	0.07	10.10	0.78
Coccolithophores	*Calyptrosphaera sphaeroidea*	RCC 1178	93	6.17	0.71	0.19	0.05	5.87	0.81
Coccolithophores	*Chrysotila dentata* (1)	PLY 378	69	9.89	0.58	0.49	0.06	6.79	0.54
Coccolithophores	*Chrysotila dentata* (2)	PLY 406	106	9.83	0.58	0.48	0.06	6.60	0.62
Coccolithophores	*Coccolithus braarudii*	RCC 1198	52	11.29	0.76	0.64	0.08	10.20	0.87
Coccolithophores	*Coccolithus pelagicus*	RCC 3776	40	10.15	0.78	0.52	0.08	10.33	0.97
Coccolithophores	*Scyphosphaera apsteinii*	RCC 3598	67	8.58	0.99	0.37	0.08	11.14	1.24
Diatoms	*Nitzchia closterium*	RCC 81	59	5.28	0.78	0.14	0.05	3.22	0.34
Diatoms	*Nitzchia sp.*	RCC 80	79	5.27	0.33	0.14	0.02	3.24	0.27
Diatoms	*Phaeodactylum tricornutum*	RCC 69	95	4.77	0.27	0.11	0.01	3.28	0.34
Diatoms	*Coscinodiscus* sp.	RCC 4273	40	14.23	1.15	1.02	0.17	11.03	1.15
Diatoms	*Halamphora coffeaeformis*	CCAP 1001/2	39	6.05	0.59	0.18	0.04	3.58	0.73
Diatoms	*Minidiscus comicus*	RCC 4660	95	5.28	0.68	0.14	0.04	2.51	0.35
Diatoms	*Minidiscus variabilis*	RCC 4657	126	5.49	0.44	0.15	0.02	2.56	0.73
Diatoms	*Skeletonema japonicum*	RCC 74	69	6.67	0.77	0.23	0.05	2.94	0.39
Diatoms	*Thalassiosira pseudonana*	RCC 950	60	5.36	0.59	0.15	0.03	2.94	0.32
Diatoms	*Thalassiosira weissflogii*	RCC 76	49	9.15	0.71	0.42	0.06	6.52	0.73
Dinoflagellates	*Amphidinium carterae*	RCC 88	157	7.65	0.80	0.30	0.06	6.31	0.61
Dinoflagellates	*Karenia papilionacea*	RCC 6516	35	12.81	1.17	0.83	0.15	12.56	1.92
Dinoflagellates	*Lepidodinium chlorophorum*	RCC 1489	34	18.11	3.74	1.71	0.70	10.20	1.32
Dinoflagellates	*Heterocapsa triquetra*	PLY 717	62	21.21	1.82	2.27	0.38	9.29	0.80
Dinoflagellates	*Prorocentrum micans*	NIES-12	13	23.07	3.98	2.73	0.93	15.05	1.81
Dinoflagellates	*Prorocentrum minimum*	PLY 714	51	12.69	1.87	0.82	0.23	7.63	1.47
Dinoflagellates	*Scripsiella trochoidea*	PLY 632	51	38.90	5.05	7.69	1.89	11.91	1.10
Dinoflagellates	*Thoracosphaera heimii*	RCC 1511	138	20.45	2.57	2.12	0.51	6.99	0.31
Eustigmatales*	*Nannochloropsis granulata*	RCC 8	50	22.06	1.85	2.45	0.41	2.25	0.46
Green algae	*Chlamydomonas concordia*	RCC 1	107	8.38	0.90	0.35	0.08	4.32	0.66
Green algae	*Dunaliella tertiolecta*	RCC 6	17	8.85	0.84	0.39	0.08	5.24	0.62
Green algae	*Bigelowiella natans*	RCC 623	269	4.84	0.43	0.12	0.02	2.41	0.33
Non-calcifying Isochrysidales	*Isochrysis galbana*	CCAP 927/1	96	9.27	4.34	0.52	0.42	3.05	0.36
Non-calcifying Isochrysidales	*Isochrysis litoralis*	RCC 1346	75	5.10	1.76	0.15	0.17	2.68	0.51
Non-calcifying Isochrysidales	*Isochrysis* sp.	RCC 4207	48	14.20	2.94	1.05	0.33	3.13	0.90
Non-calcifying Isochrysidales	*Ruttnera* sp.	RCC 3696	70	5.30	2.23	0.16	0.21	3.04	0.37
Pavlovales	*Diacronema vlkianum* (1)	RCC 1546	103	13.22	0.32	0.87	0.04	2.82	0.39
Pavlovales	*Diacronema vlkianum* (2)	RCC 3780	49	10.90	1.11	0.60	0.10	2.81	0.33
Pavlovales	*Pavlova granifera*	RCC 1557	117	15.03	2.99	1.17	0.42	3.55	0.52
Phaeocystales*	*Phaeocystis globosa*	RCC 678	110	7.22	0.33	0.26	0.02	2.90	0.37
Picophytoplankton	*Micromonas pusilla*	RCC 1614	121	5.08	0.18	0.13	0.01	1.23	0.06

Picophytoplankton	*Osteococcus tauri*	RCC 4221	93	4.01	0.53	0.08	0.02	1.05	0.01
Picophytoplankton	*Synechococcus* sp. (1)	RCC 1084	42	5.27	0.63	0.14	0.03	0.90	0.05
Picophytoplankton	*Synechococcus* sp. (2)	RCC 2570	8	4.49	0.20	0.10	0.01	0.92	0.07
Prymnesiales	*Chrysochromulina camella*	RCC 1185	114	7.31	0.74	0.27	0.05	5.41	0.79
Prymnesiales	*Chrysochromulina* sp.	RCC 656	107	6.96	0.39	0.24	0.03	2.66	0.28
Prymnesiales	*Prymnesium parvum*	RCC 191	172	6.00	0.29	0.18	0.02	3.58	0.39
TOTAL			**4884**						

Table S4. A summary of the predictor variables derived at the group level, with the unbalanced dataset (i.e. variable *n* across the strains within each group). *denotes groups that were just represented by a single species.

Group	***n***	**t_{50} (s)**	**SD t_{50}**	**Charge at t_{50} (mC)**	**SD Charge at t50**	**effective radius (µm)**	**SD effective radius**
Calcifying Isochrysidales	1271	16.27	3.15	1.37	0.48	3.38	0.76
Coccolithophores	593	8.81	1.80	0.40	0.15	7.85	2.17
Diatoms	711	6.20	2.31	0.22	0.22	3.65	2.11
Dinoflagellates	541	17.25	9.26	1.92	2.15	8.33	2.53
Eustigmatales*	50	22.06	1.85	2.45	0.41	2.25	0.46
Green algae	393	5.98	1.79	0.19	0.12	3.05	1.07
Non-calcifying Isochrysidales	289	8.05	4.53	0.43	0.45	2.97	0.55
Pavlovales	269	13.59	2.53	0.95	0.35	3.14	0.57
Phaeocystales*	110	7.22	0.33	0.26	0.02	2.90	0.37
Picophytoplankton	264	4.72	0.68	0.11	0.03	1.11	0.14
Prymnesiales	393	6.64	0.76	0.22	0.05	3.86	1.18
TOTAL	**4884**						

Table S5. A summary of the predictor variables derived at the strain level, with the balanced dataset (i.e. standardised *n* across the strains within each group, see Methods).

Group	Species detail	Strain	*n*	t_{50} (s)	SD t_{50}	Charge at t_{50} (mC)	SD Charge at t50	effective radius (µm)	SD effective radius
Calcifying Isochrysidales	*Emiliania huxleyi,* non-calcified haploid	RCC 1217	80	14.01	3.61	1.04	0.41	2.76	0.64
Calcifying Isochrysidales	*Emiliania huxleyi,* morphotype A,light - moderately calcified	RCC 911	80	16.92	1.51	1.44	0.27	3.30	0.37
Calcifying Isochrysidales	*Emiliania huxleyi,* morphotype A, moderately calcified	RCC 1731	80	16.96	0.89	1.44	0.16	3.43	0.33
Calcifying Isochrysidales	*Emiliania huxleyi,* morphotype A/R, over-calcified with bulkycentre	PLY 853	80	15.01	0.95	1.13	0.15	2.66	0.22
Calcifying Isochrysidales	*Emiliania huxleyi* morphotype A/R, over-calcified shields	RCC 1216	80	17.01	2.51	1.48	0.39	3.34	0.23
Calcifying Isochrysidales	*Emiliania huxleyi,* non-calcified diploid	RCC 1242	80	21.21	2.44	2.28	0.49	2.90	0.52
Calcifying Isochrysidales	*Gephyrocapsa oceanica*	RCC 1314	80	14.19	4.98	1.13	0.81	5.11	0.53
Coccolithophores	*Calcidiscus leptoporus* (1)	RCC 1130	40	7.13	0.91	0.26	0.06	6.26	0.74
Coccolithophores	*Calcidiscus leptoporus* (2)	RCC 1150	40	10.15	0.68	0.52	0.07	10.13	0.76
Coccolithophores	*Calyptrosphaera sphaeroidea*	RCC 1178	40	6.37	0.87	0.21	0.06	5.96	0.91
Coccolithophores	*Chrysotila dentata* (1)	PLY 378	40	9.92	0.62	0.49	0.06	6.83	0.57
Coccolithophores	*Chrysotila dentata* (2)	PLY 406	40	9.78	0.58	0.48	0.06	6.67	0.80
Coccolithophores	*Coccolithus braarudii*	RCC 1198	40	11.31	0.66	0.64	0.07	10.23	0.84
Coccolithophores	*Coccolithus pelagicus*	RCC 3776	40	10.15	0.78	0.52	0.08	10.33	0.97
Coccolithophores	*Scyphosphaera apsteinii*	RCC 3598	40	8.55	1.06	0.37	0.09	11.03	1.30
Diatoms	*Nitzchia closterium*	RCC 81	39	5.15	0.76	0.14	0.04	3.23	0.37
Diatoms	*Nitzchia* sp.	RCC 80	39	5.28	0.30	0.14	0.02	3.24	0.25
Diatoms	*Phaeodactylum tricornutum*	RCC 69	39	4.75	0.24	0.11	0.01	3.27	0.29
Diatoms	*Coscinodiscus* sp.	RCC 4273	39	14.21	1.16	1.02	0.17	11.03	1.17
Diatoms	*Halamphora coffeaeformis*	CCAP 1001/2	39	6.05	0.59	0.18	0.04	3.58	0.73
Diatoms	*Minidiscus comicus*	RCC 4660	39	5.42	0.72	0.15	0.04	2.56	0.39
Diatoms	*Minidiscus variabilis*	RCC 4657	39	5.58	0.39	0.16	0.02	2.46	0.29
Diatoms	*Skeletonema japonicum*	RCC 74	39	6.80	0.77	0.23	0.05	2.93	0.38
Diatoms	*Thalassiosira pseudonana*	RCC 950	39	5.36	0.59	0.15	0.03	2.95	0.34
Diatoms	*Thalassiosira weissflogii*	RCC 76	39	9.25	0.56	0.43	0.05	6.57	0.61
Dinoflagellates	*Amphidinium carterae*	RCC 88	13	7.84	0.87	0.31	0.07	6.44	0.71
Dinoflagellates	*Karenia papilionacea*	RCC 6516	13	12.78	0.78	0.82	0.10	12.55	1.61
Dinoflagellates	*Lepidodinium chlorophorum*	RCC 1489	13	18.68	3.72	1.81	0.70	10.12	1.66
Dinoflagellates	*Heterocapsa triquetra*	PLY 717	13	21.30	1.93	2.29	0.41	9.30	0.60
Dinoflagellates	*Prorocentrum micans*	NIES-12	13	23.07	3.98	2.73	0.93	15.05	1.81
Dinoflagellates	*Prorocentrum minimum*	PLY 714	13	13.35	1.92	0.91	0.25	8.05	1.39
Dinoflagellates	*Scripsiella trochoidea*	PLY 632	13	38.54	6.86	7.64	2.49	11.83	0.95
Dinoflagellates	*Thoracosphaera heimii*	RCC 1511	13	20.46	2.71	2.13	0.54	6.88	0.18
Eustigmatales*	*Nannochloropsis granulata*	RCC 8	50	22.06	1.85	2.45	0.41	2.25	0.46

Green algae	*Chlamydomonas concordia*	RCC 1	17	8.26	1.09	0.35	0.09	4.33	0.67
Green algae	*Dunaliella tertiolecta*	RCC 6	17	8.85	0.84	0.39	0.08	5.24	0.62
Green algae	*Bigelowiella natans*	RCC 623	17	4.75	0.44	0.11	0.02	2.55	0.37
Non-calcifying Isochrysidales	*Isochrysis galbana*	CCAP 927/1	48	8.78	4.30	0.48	0.41	3.05	0.37
Non-calcifying Isochrysidales	*Isochrysis litoralis*	RCC 1346	48	4.98	1.56	0.14	0.16	2.57	0.55
Non-calcifying Isochrysidales	*Isochrysis* sp.	RCC 4207	48	14.20	2.94	1.05	0.33	3.13	0.90
Non-calcifying Isochrysidales	*Ruttnera* sp.	RCC 3696	48	5.11	1.94	0.15	0.18	3.06	0.38
Pavlovales	*Diacronema vlkianum* (1)	RCC 1546	49	13.24	0.31	0.88	0.04	2.90	0.36
Pavlovales	*Diacronema vlkianum* (2)	RCC 3780	49	10.90	1.11	0.60	0.10	2.81	0.33
Pavlovales	*Pavlova granifera*	RCC 1557	49	15.00	2.96	1.17	0.42	3.58	0.45
Phaeocystales*	*Phaeocystis globosa*	RCC 678	110	7.22	0.33	0.26	0.02	2.90	0.37
Picophytoplankton	*Micromonas pusilla*	RCC 1614	8	5.10	0.15	0.13	0.01	1.23	0.05
Picophytoplankton	*Osteococcus tauri*	RCC 4221	8	3.86	0.73	0.08	0.03	1.05	0.01
Picophytoplankton	*Synechococcus* sp. (1)	RCC 1084	8	5.31	0.66	0.14	0.03	0.89	0.06
Picophytoplankton	*Synechococcus* sp. (2)	RCC 2570	8	4.49	0.20	0.10	0.01	0.92	0.07
Prymnesiales	*Chrysochromulina camella*	RCC 1185	107	7.30	0.74	0.27	0.05	5.41	0.80
Prymnesiales	*Chrysochromulina* sp.	RCC 656	107	6.96	0.39	0.24	0.03	2.66	0.28
Prymnesiales	*Prymnesium parvum*	RCC 191	107	6.02	0.32	0.18	0.02	3.61	0.39
TOTAL			**2277**						

Table S6. A summary of the predictor variables derived at the group level, with the balanced dataset (i.e. standardised *n* across the strains within each group, see Methods). *denotes groups that were just represented by a single species.

Group	***n***	**t_{50} (s)**	**SD t_{50}**	**Charge at t_{50} (mC)**	**SD Charge at t50**	**effective radius (µm)**	**SD effective radius**
Calcifying Isochrysidales	560	16.47	3.59	1.42	0.58	3.36	0.88
Coccolithophores	320	9.17	1.76	0.44	0.15	8.43	2.21
Diatoms	390	6.79	2.84	0.27	0.27	4.18	2.59
Dinoflagellates	104	19.50	9.30	2.33	2.37	10.03	3.04
Eustigmatales*	50	22.06	1.85	2.45	0.41	2.25	0.46
Green algae	51	7.29	2.00	0.29	0.14	4.04	1.26
Non-calcifying Isochrysidales	192	8.27	4.73	0.45	0.47	2.95	0.63
Pavlovales	147	13.05	2.48	0.88	0.34	3.10	0.51
Phaeocystales*	110	7.22	0.33	0.26	0.02	2.90	0.37
Picophytoplankton	32	4.69	0.75	0.11	0.03	1.02	0.15
Prymnesiales	321	6.76	0.75	0.23	0.05	3.89	1.26
TOTAL	**2277**						

Table S7. Results from training the random forest using 80% of the unbalanced data for the key groups only (n = 3880). The green highlighted grid squares indicate the number of successful categorisations for each group within the training. Overall "out-of-bag" error was 9.14% (thus 90.86% overall accuracy).

		Actual (Testing)				
		Calcifying Isochrysidales	Coccolithophores	Diatoms	Dinoflagellates	Picophytoplankton
Predicted (Testing)	Calcifying Isochrysidales	282	1	2	0	0
	Coccolithophores	4	96	6	21	0
	Diatoms	3	5	118	4	0
	Dinoflagellates	1	19	5	90	0
	Picophytoplankton	0	0	0	0	52
	Accuracy (%)	97.24	79.34	90.08	78.26	100
	Overall Accuracy (%)	89.99				

Table S8. Results from testing the trained random forest using a random subset of 20% of the unbalanced data for the key groups only (n = 3880). The green highlighted grid squares indicate the number of successful categorisations for each group within the training.

		Predicted (Training)					
		Calcifying Isochrysidales	Coccolithophores	Diatoms	Dinoflagellates	Picophytoplankton	Accuracy (%)
Actual (Training)	Calcifying Isochrysidales	962	4	10	5	0	98.06
	Coccolithophores	0	401	18	53	0	84.96
	Diatoms	5	35	517	23	0	89.14
	Dinoflagellates	7	64	20	335	0	78.64
	Picophytoplankton	0	0	0	0	212	100
						Overall Accuracy (%)	90.86

Table S9. Results from testing the trained random forest using a random subset of 20% of the balanced data for the key groups only (n = 1406). The green highlighted grid squares indicate the number of successful categorisations for each group within the training.

		Actual (Testing)				
		Calcifying Isochrysidales	Coccolithophores	Diatoms	Dinoflagellates	Picophytoplankton
Predicted (Testing)	Calcifying Isochrysidales	124	1	2	0	0
	Coccolithophores	1	66	3	4	0
	Diatoms	1	8	80	6	0
	Dinoflagellates	0	1	3	14	0
	Picophytoplankton	0	0	0	0	6
	Accuracy (%)	98.41	86.84	90.91	58.33	100.00
	Overall Accuracy (%)	90.63				

Table S10. Results from training the random forest using 80% of the unbalanced data for all the groups (n = 4884). The green highlighted grid squares indicate the number of successful categorisations for each group within the training. Overall "out-of-bag" error was 28.12% (thus 71.88 % overall accuracy).

		Predicted (Training)											
		Calcifying Isochrysidales	Coccolithophores	Diatoms	Dinoflagellates	Eustigmatales*	Green algae	Non-calcifying Isochrysidales	Pavlovales	Phaeocystales*	Picophytoplankton	Prymnesiales	Accuracy (%)
Actual (Training)	Calcifying Isochrysidales	886	4	2	4	5	20	20	37	0	0	3	90.32
	Coccolithophores	1	393	13	50	0	0	0	0	0	0	15	83.26
	Diatoms	3	30	344	21	0	63	40	1	9	0	69	59.31
	Dinoflagellates	4	61	15	329	0	4	0	0	0	0	13	77.23
	Eustigmatales*	12	0	0	0	30	0	0	0	0	0	0	71.43
	Green algae	12	2	88	0	0	168	29	0	4	0	11	53.5
	Non-calcifying Isochrysidales	52	0	83	1	0	26	47	16	1	0	1	20.7
	Pavlovales	68	0	2	1	0	1	7	132	1	0	2	61.68
	Phaeocystales*	0	0	11	0	0	5	0	1	53	0	22	57.61
	Picophytoplankton	0	0	0	0	0	0	0	0	0	208	0	100
	Prymnesiales	0	20	49	19	0	7	1	2	27	0	199	61.42
												Overall Accuracy (%)	71.88

Table S11. Results from testing the trained random forest using a random subset of 20% of the unbalanced data for all the groups (n = 4884). The green highlighted grid squares indicate the number of successful categorisations for each group within the training.

		Actual (Testing)										
		Calcifying Isochrysidales	Coccolithophores	Diatoms	Dinoflagellates	Eustigmatales*	Green algae	Non-calcifying Isochrysidales	Pavlovales	Phaeocystales*	Picophytoplankton	Prymnesiales
Predicted (Testing)	Calcifying Isochrysidales	254	2	1	0	2	2	14	16	0	0	0
	Coccolithophores	3	91	6	19	0	0	0	0	0	0	0
	Diatoms	1	5	72	4	0	14	24	0	1	0	3
	Dinoflagellates	1	15	5	86	0	1	0	0	0	0	5
	Eustigmatales*	1	0	0	0	6	0	0	0	0	0	0
	Green algae	8	2	20	0	0	51	2	1	1	0	1
	Non-calcifying Isochrysidales	8	0	9	0	0	6	14	0	0	0	0
	Pavlovales	12	0	0	0	0	1	4	38	0	0	0
	Phaeocystales*	0	0	2	0	0	2	1	0	8	0	4
	Picophytoplankton	0	0	0	0	0	0	0	0	0	56	0
	Prymnesiales	2	6	16	6	0	2	3	0	8	0	56
	Accuracy (%)	87.59	75.21	54.96	74.78	75	64.56	22.58	69.09	44.44	100	81.16
	Overall Accuracy (%)	72.91										

Table S12. Results from testing the trained random forest using a random subset of 20% of the balanced data for all the groups (*n* = 2277). The green highlighted grid squares indicate the number of successful categorisations for each group within the training.

		Actual (Testing)										
		Calcifying Isochrysidales	Coccolithophores	Diatoms	Dinoflagellates	Eustigmatales*	Green algae	Non-calcifying Isochrysidales	Pavlovales	Phaeocystales*	Picophytoplankton	Prymnesiales
Predicted (Testing)	Calcifying Isochrysidales	113	0	0	0	4	2	5	3	0	0	0
	Coccolithophores	1	61	3	3	0	0	0	0	0	0	4
	Diatoms	0	5	54	7	0	2	16	0	1	0	5
	Dinoflagellates	0	0	3	14	0	0	0	0	0	0	0
	Eustigmatales*	2	0	0	0	7	0	0	0	0	0	0
	Green algae	2	1	1	0	0	4	0	0	0	0	1
	Non-calcifying Isochrysidales	5	0	8	0	0	1	19	0	0	0	0
	Pavlovales	3	0	1	0	0	0	3	20	0	0	1
	Phaeocystales*	0	0	6	0	0	0	1	0	12	0	7
	Picophytoplankton	0	0	0	0	0	0	0	0	0	3	0
	Prymnesiales	0	9	12	0	0	0	0	0	9	0	40
	Accuracy (%)	89.68	80.26	61.36	58.33	63.64	44.44	43.18	86.96	54.55	100	68.97
	Overall Accuracy (%)	71.69										

Table S13. Summary of the model comparison for fitting linear models to log(charge at t_{50}) against log(effective radius), across all the full balanced dataset (*n* = 2277), see Figure 4 (Main tesxt). The best model (lowest AIC) is the mixed model, including the random effect of grouping on the slope and intercept of the response. This indicates that there is an overall significant positive size scaling, but that the relationship differs across the groups (See Figure S8)

	npar	AIC	BIC	logLik	deviance	Chisq	Df	Pr(>Chisq)
lm_size_dep	3	6408.995	6426.187	-3201.5	6402.995			
lmer_size_dep2	**6**	**3336.871**	**3371.254**	**-1662.44**	**3324.871**	**3078.124**	**3**	**<2.2 x 10^{-16}**

Models:
lm_size_dep: ln_mC ~ ln_rad
lmer_size_dep2: ln_mC ~ ln_rad + (ln_rad | eco_group)

Table S14: Linear model output for each of the group specific relationships (see Figure S8). Bold highlights indicate a significant allometric scaling, using *p* values for the slope coefficient only. 'Lower' and 'Upper' represent the 95% confidence intervals of the intercept and slope ('ln_rad') coefficients. The overall size scaling is visualised in Figure 4 (Main text). *denotes groups that were just represented by a single species.

	(Intercept)	lower	upper	ln_rad	lower	upper	*p* (slope only)
Calcifying Isochrysidales	0.64	0.43	0.84	**-0.33**	**-0.50**	**-0.16**	**0.000189**
Coccolithophores	-2.85	-3.27	-2.42	**0.93**	**0.73**	**1.13**	**0.000000**
Diatoms	-3.24	-3.39	-3.10	**1.26**	**1.16**	**1.37**	**0.000000**
Dinoflagellates	-2.90	-3.62	-2.18	**1.47**	**1.16**	**1.79**	**0.000000**
Eustigmatales*	0.77	0.20	1.34	0.15	-0.55	0.84	0.682133
Green algae	-3.61	-4.16	-3.05	**1.64**	**1.23**	**2.04**	**0.000000**
Non-calcifying Isochrysidales	-2.43	-2.83	-2.04	**1.00**	**0.63**	**1.36**	**0.000000**
Pavlovales	-1.57	-2.13	-1.01	**1.23**	**0.73**	**1.72**	**0.000001**
Phaeocystales*	-1.60	-2.38	-0.83	0.24	-0.49	0.97	0.519235
Picophytoplankton	-2.23	-2.40	-2.06	-0.28	-1.51	0.95	0.655836
Prymnesiales	-1.81	-2.04	-1.58	**0.24**	**0.07**	**0.42**	**0.005498**
Overall (lmer model)	-1.87	-2.78	-0.97	**0.76**	**0.34**	**1.16**	NA

Table S15. A summary of the Pairwise Wilcoxon Rank Sum testing, to complement Figure. 5 (Main text). Bold text indicates a significant difference ($p < 0.05$) in the mC/µm values between the pairs.

Group1	Group2	*p* value (Bonferroni adjusted for nonparametric data)
Coccolithophores	**Calcifying Isochrysidales**	**0.000000**
Diatoms	**Calcifying Isochrysidales**	**0.000000**
Dinoflagellates	**Calcifying Isochrysidales**	**0.000000**
Eustigmatales*	**Calcifying Isochrysidales**	**0.000000**
Green algae	**Calcifying Isochrysidales**	**0.000000**
Non-calcifying Isochrysidales	**Calcifying Isochrysidales**	**0.000000**
Pavlovales	**Calcifying Isochrysidales**	**0.000000**
Phaeocystales*	**Calcifying Isochrysidales**	**0.000000**
Picophytoplankton	**Calcifying Isochrysidales**	**0.000000**
Prymnesiales	**Calcifying Isochrysidales**	**0.000000**
Diatoms	Coccolithophores	0.065059
Dinoflagellates	**Coccolithophores**	**0.000000**
Eustigmatales*	**Coccolithophores**	**0.000000**
Green algae	**Coccolithophores**	**0.000156**
Non-calcifying Isochrysidales	Coccolithophores	0.746392
Pavlovales	**Coccolithophores**	**0.000000**
Phaeocystales*	**Coccolithophores**	**0.000000**
Picophytoplankton	**Coccolithophores**	**0.000000**
Prymnesiales	**Coccolithophores**	**0.000000**

Dinoflagellates	**Diatoms**	**0.000000**
Eustigmatales*	**Diatoms**	**0.000000**
Green algae	Diatoms	0.145827
Non-calcifying Isochrysidales	Diatoms	1.000000
Pavlovales	**Diatoms**	**0.000000**
Phaeocystales*	**Diatoms**	**0.000000**
Picophytoplankton	**Diatoms**	**0.000000**
Prymnesiales	**Diatoms**	**0.005529**
Eustigmatales*	**Dinoflagellates**	**0.000000**
Green algae	**Dinoflagellates**	**0.000000**
Non-calcifying Isochrysidales	**Dinoflagellates**	**0.000016**
Pavlovales	**Dinoflagellates**	**0.000001**
Phaeocystales*	**Dinoflagellates**	**0.000009**
Picophytoplankton	Dinoflagellates	0.423199
Prymnesiales	**Dinoflagellates**	**0.000000**
Green algae	**Eustigmatales***	**0.000000**
Non-calcifying Isochrysidales	**Eustigmatales***	**0.000000**
Pavlovales	**Eustigmatales***	**0.000000**
Phaeocystales*	**Eustigmatales***	**0.000000**
Picophytoplankton	**Eustigmatales***	**0.000000**
Prymnesiales	**Eustigmatales***	**0.000000**
Non-calcifying Isochrysidales	Green algae	1.000000
Pavlovales	**Green algae**	**0.000000**
Phaeocystales*	**Green algae**	**0.000000**
Picophytoplankton	**Green algae**	**0.000000**
Prymnesiales	Green algae	1.000000
Pavlovales	**Non-calcifying Isochrysidales**	**0.000000**
Phaeocystales*	**Non-calcifying Isochrysidales**	**0.000749**
Picophytoplankton	Non-calcifying Isochrysidales	0.859688
Prymnesiales	Non-calcifying Isochrysidales	1.000000
Phaeocystales*	**Pavlovales**	**0.000000**
Picophytoplankton	**Pavlovales**	**0.000000**
Prymnesiales	**Pavlovales**	**0.000000**
Picophytoplankton	**Phaeocystales***	**0.000291**
Prymnesiales	**Phaeocystales***	**0.000000**
Prymnesiales	**Picophytoplankton**	**0.000000**
Overal Kruskall Wallis for significant effect of group		**$<2.2 \times 10^{-16}$**

Table S16 . A summary of the Pairwise Wilcoxon Rank Sum testing, to complement Figure. 6b (Main text), showing the difference in natural log(mC/µm) across the different *Emiliania huxleyi* strains in this study. Bold text indicates a significant difference ($p < 0.05$) in the mC/µm values between the pairs. The non-calcified diploid strain of *E. huxelyi* is significantly different to all other strains.

Group 1	Group 2	*p* value (Bonferroni adjusted for nonparametric data)
Morphotype A, moderately calcified (1731)	Morphotype A, light to moderately calcified (911)	1.000000
Morphotype A/R, over-calcified shields (1216)	Morphotype A, light to moderately calcified (911)	0.315877
Morphotype A/R, over-calcified, bulky centre (PLY853)	Morphotype A, light to moderately calcified (911)	1.000000
Non-calcified, diploid (1242)	**Morphotype A, light to moderately calcified (911)**	**0.000000**
Non-calcified, Haploid (1217)	Morphotype A, light to moderately calcified (911)	0.785559
Morphotype A/R, over-calcified shields (1216)	**Morphotype A, moderately calcified (1731)**	**0.011631**
Morphotype A/R, over-calcified, bulky centre (PLY853)	Morphotype A, moderately calcified (1731)	1.000000
Non-calcified, diploid (1242)	**Morphotype A, moderately calcified (1731)**	**0.000000**
Non-calcified, Haploid (1217)	Morphotype A, moderately calcified (1731)	1.000000
Morphotype A/R, over-calcified, bulky centre (PLY853)	**Morphotype A/R, over-calcified shields (1216)**	**0.008142**
Non-calcified, diploid (1242)	**Morphotype A/R, over-calcified shields (1216)**	**0.000000**
Non-calcified, Haploid (1217)	**Morphotype A/R, over-calcified shields (1216)**	**0.004862**
Non-calcified, diploid (1242)	**Morphotype A/R, over-calcified, bulky centre (PLY853)**	**0.000000**
Non-calcified, Haploid (1217)	Morphotype A/R, over-calcified, bulky centre (PLY853)	0.353355
Non-calcified, Haploid (1217)	**Non-calcified, diploid (1242)**	**0.000000**
Overal krusfall wallis for effect of *Emiliania huxleyi* strain type		**<2.2 x 10-16**

References

Guillard, R. R. L., and P. E. Hargraves. 1993. Stichochrysis immobilis is a diatom, not a chrysophyte. Phycologia **32**: 234–236. doi:10.2216/i0031-8884-32-3-234.1

Guillard, R. R. L., and J. H. Ryther. 1962. STUDIES OF MARINE PLANKTONIC DIATOMS: I. CYCLOTELLA NANA HUSTEDT, AND DETONULA CONFERVACEA (CLEVE) GRAN. Can J Microbiol **8**: 229–239. doi:10.1139/m62-029

Keller, M. D., R. C. Selvin, W. Claus, and R. R. L. Guillard. 1987. MEDIA FOR THE CULTURE OF OCEANIC ULTRAPHYTOPLANKTON. J Phycol **23**: 633–638. doi:10.1111/j.1529-8817.1987.tb04217.x

Morel, F. M. M., J. G. Rueter, D. M. Anderson, and R. R. L. Guillard. 1979. AQUIL: A CHEMICALLY DEFINED PHYTOPLANKTON CULTURE MEDIUM FOR TRACE METAL STUDIES 1 2 . J Phycol **15**: 135–141. doi:10.1111/j.1529-8817.1979.tb02976.x